U S

Universitetet
i Stavanger

FACULTY OF SCIENCE AND TECHNOLOGY

MASTER THESIS

Study program/specialization: **Engineering structures and Materials w/specialization in Mechanical Structures**	**Spring semester, 2019** **Open**/~~Confidential~~
Author: **Alexandra Bjørkli**	*Alexandra Bjørkli* .... (signature of author)

Supervisor: **Dr. Knut Erik T. Giljarhus**	

Title of master's thesis: **T-junctions in a hydronic system**	

| Credits (ECT): **30**	
Keywords: **Mesh** **T-junction** **Flow in branch pipe** **Bifurcation** **Computational Fluid Dynamics (CFD)**	Number of pages: ………56………… + supplemental material/other: ………… Stavanger, 15.06.2019 date/year

Title page for Master Thesis
Faculty of Science and Technology

MSc ENGINEERING STRUCTURES AND MATERIALS

MASTER THESIS

T-junctions in a hydronic system

AUTHOR:

Alexandra Bjørkli
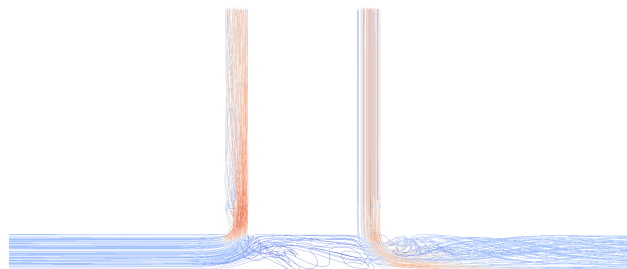
Acknowledgements

I like to thank Dr. Knut Erik Giljarhus and Gether AS for this opportunity. And a special thank to Dr. Knut Erik Giljarhus for the guidance, patience and support during all stages of this thesis.

I would also thank my family for the support they have given during the time I have spent on the thesis.

Abstract

The OpenFoam software with the Computational Fluid Dynamics (CFD) theory is used in this thesis. In this paper the importance of grid resolution and layers are shown. Four different grid resolutions with about 30& reduction each time on the original cell amount with or without layers are compared. The applicability of Reynolds Average Navier-Stokes (RANS) Shear Stress Transport (SST) $k-\omega$ model on the turbulent flow in a T-junction are investigated. There is done a validation study on the T-junction with indirect comparison to an experiment preformed by the collaboration of OECD/NEA and Vattenfall Research and Development at the Älvkarleby Laboratory in Sweden. The effect two adjacent branches in a T-junction have on each other is also looked into. A double T-junction with different spacing, 600mm, 2.5D, 2D and 1.5D, between are simulated. The comparisons are done visual by looking at the flow profile, stream tracers, surface lic and the bulk velocity in the middle of the branches. It was found that the best configuration that disturb the recirculation zone the least is between 2 and 2.5D for this case when the closeness of the branches are of importance.

Contents

Acronyms

CFD Computational Fluid Dynamics

DNS Direct Numerical Simulation

GAMG Geometric Algebraic Multi-Grid

LDA Laser Doppler Anemometer

LES Large Eddy Simulation

PIV Particle Image Velocimetry

RANS Reynolds Average Navier-Stokes

RAS Reynolds Averaged Simulation

RSM Reynolds Stress Models

SGS Sub Grid Scale

SIMPLE Semi-Implicit Method for Pressure Linked Equations

SST Shear Stress Transport

List of Figures

List of Tables

1   Introduction

It's not the first time the T-junction has been studied. Due to the danger of thermal striping, this subject becomes very relevant in the industry when it comes to designing systems where thermal stresses would lead to failure. The effect of turbulence will also take it toll on the pipe construction. In this paper the focus is more on the energy loss through velocity, not on the temperature fluctuation.

Gether AS is a company that has a main goal to make substantial energy solutions on a large base. The company wants to be a long term contractor for delivery of substantial energy- and performance-systems [1].

Gether AS has build a compact geothermal-hydronic heating and cooling system for use in office buildings and residential neighborhoods. By the use of the geothermal temperature they designed an unique system that can extract, store and transport heat and cold. Since the prototype of the system is already built, the company wants a CFD simulation for verification and potentially improvements of the energy loss in the central.

For the first part one will look at a T-junction with a conventional flow, two inlets and one outlet that's in the main pipe. The second part will take a closer look at a T-junction with outflow in the branch pipe. Before finally examining the whole branching system designed by Gether as.

Hydronic is a cooling or heating system in which heat or cold is transported using circulating water. Perhaps the most known heating medium is water, steam or oil in radiators.

The main objective of this paper is to perform CFD validation test cases and a parametric study of T-junction systems. To quantify and potentially improve the flow in the cross sections of the t-junctions for future developments for Gether AS.

2 Method

There are three different methods used in CFD

- Direct Numerical Simulation (DNS)

- Large Eddy Simulation (LES)

- RANS or Reynolds Averaged Simulation (RAS)

The DNS method has a high computational cost and therefore claim a lot of computer resources. Because of the very high expense connected to this simulation, only large companies can afford it at this time. DNS compute both mean flow and all turbulence velocity fluctuations. It solves the instantaneous continuity and the Navier-Stokes equations by using small scale mesh with small time steps to resolve even the smallest turbulent eddies. It needs complete time resolution to solves where energy dissipation takes place and periods of fastest fluctuations. There fore DNS can give precise details at any point in the flow. This leads to the redundancy of the turbulence models [2].

The LES method is widely used in the scientific community. Even though it demands a lot of computer resources, the computational cost is far less than the DNS. The simulation filters out the larger eddies and include the the smaller eddies in the Sub Grid Scale (SGS) stresses. These stresses develops from the interactions between larger resolved and smaller unresolved eddies. The resolved flow is described by the larger eddies and the mean SGS stresses.

The RANS method or also called the RAS method has the lowest computational cost, and therefore might be the less accurate choice in some cases. However, this is a widely used approach, so there are several validation cases that strengthen the confidence in this simulation [3]. It uses the average velocities and pressure fields in the Navier-Stokes equation. As a result of time averaging, the interactions between various turbulence fluctuations creates an extra term that is modelled with the classical turbulence models.

There are 3 different RANS-based turbulence models [4]:

1. Linear eddy viscosity models

2. Nonlinear eddy viscosity

3. Reynolds Stress Models (RSM)

Linear eddy viscosity models are turbulence models which use a linear relationship between the mean flow straining field and the Reynolds stresses. The Reynolds stresses are attrived from Reynolds averaging of the Navier-Stokes equations [4].

Linear eddy viscosity models have three subcategories that are differentiated after the number of transport equations that are used to arrive to the eddy viscosity coefficient [4]:

- Algebraic models

- One equation models

- Two equation models

The Boussinesq eddy viscosity assumption, assumes that the Reynolds stress tensor, τ_{ij}, is proportional to the mean strain rate tensor, S_{ij}. This assumption works for simple flows like straight boundary layers and wakes. Flows with heavy rotations, significant curvature and stagnation flow presents no validation with two equation models [4].

2.1 The k-ϵ model

Two equation models are models that include two extra transport equations to represent the turbulent properties of the flow. The turbulent kinetic energy, k, is most often one of them. The turbulent dissipation, ϵ, gives the length scale, and with the combination of the transport equations k and ϵ, one gets the standard k-ϵ model from Launder and Spalding [5].

There are several different models, the k-ϵ model, from the Linear eddy viscosity model, and the Reynolds stress model, which has seven extra transport equations, are perhaps two of the most common. The k-ϵ model is known to give good results for a wide variety of thin shear layers and recirculation flows without constant model adjustments. It especially achieve good results in confined flows where there are emphasis on the Reynolds stresses. The k-ϵ model is a simple turbulence model that only need initial and/or boundary conditions. Due to these advantages it is probably the reasons for that this model is widely used and the most validated turbulence model [2]. Even though it is widely used, it is weak in cases with large adverse pressure gradients [4], and gives moderate agreements in unconfined flows. The tendency to highly overpredict in weak shear layers, like far wakes and mixing layers, and in stagnation areas are high [2]. The k-ϵ model has had several modifications over time that have lead to other turbulence models with their basis from the k-ϵ model.

2.2 The k-ω model

One of these adjustments from the k-ϵ model is the Wilcox k-ω turbulence model [6]–[9]. In this model one exchanges the ϵ transport equation with the ω transport equation, $\omega = \epsilon/k$. The specific turbulence dissipation rate, ω, gives a time scale to this two-equation eddy-viscosity model.

In situations with low Reynolds numbers, the integration to the wall does not require wall-damping function. The turbulent kinetic energy, k, and the wall is both set to zero, while ω needs to be of a non zero value. At the boundary conditions, the inlet values of k and ω must be specified, while for the outlet the zero gradient choice is usually used. A major weakness of the k-ω model is the sensitivity to the free-stream turbulence properties. This makes it extremely problematic to use in aerodynamic and aerospace cases [2].

2.3 The SST k-ω turbulence model

With the SST k-ω model one get the combination of both the k-ϵ and the k-ω models. Menter [10]–[13] utilized the advantages of the $k - \epsilon$ model's lower sensitivity to the assumed values in free stream. At the same time, Menter avoided the negative aspect of boundary layers with adverse pressure gradients, by switching to the $k - \omega$ model in the near wall region. By transforming the ϵ-equation into the ω-equation by the use of $\epsilon = k\omega$, the ω transport equation requires an extra source term, the cross-diffusion term. The Reynold stress computation and the k equation uses the same approach as in Wilcos's original $k - \omega$ model.

Because of the k-ω formulation, this model can be used as a Low-Re turbulence model without any extra damping function. It uses the inner parts of the boundary layer all the way down to the wall through the viscous sub-layer. In free-stream the SST k-ω model switches to k-ϵ formulation to get less sensitivity to the inlet free-stream turbulence properties as mentioned above. The SST k-ω model performs well in adverse pressure gradients and separating flow. On the downside, the model produce a bit too high turbulence levels in regions with large normal strain. These will be regions with stagnation and strong acceleration [4].

In 2003, Menter [14] made modifications to the SST $k - \omega$ model based on experiments with the model in general-purpose computation. The highlights of these modifications are revived model constants, blending functions and limiters. To avoid numerical instability due to the difference of the eddy viscosity derived by the standard k - ϵ used in the far field, and the transformed k - ϵ near the wall, the SST k - ω uses blending functions. In addition to smoothing the cross-diffusion term, the blending function can also be used for a model constant. The limiters are set to prevent the build-up of turbulence in stagnation regions and to limit the eddy viscosity to give improved performance in flows with adverse pressure gradients and wake regions.

3   Governing equation

The governing equations of fluids states the conservation of:

- Mass

- Momentum

- Energy

Assumptions:

- incompressible

- steady state

- turbulence

Liquids and gases flowing at low speeds are considered incompressible. Due to no variation in density for incompressible fluids, there are no direct links between the energy equation to the other two equations, conservation of mass and momentum equations. By the use of equation of state one can link the energy equation to the other two equations. Pressure and temperature variations may lead to density variations. Only when heat transfer is present one needs to solve the energy equation along with the conservation of mass and momentum equations.

The continuity equation of mass conservation:

$$\frac{\partial \rho}{\partial t} + div(\rho \mathbf{u}) = 0 \tag{1}$$

The continuity equation for the mean flow:

$$div \ \mathbf{U} = 0 \tag{2}$$

Since the T-junction is heat insulated, the heat flux in this case becomes zero:

$$- div \ \mathbf{q} = 0 \tag{3}$$

In incompressible flows, there are no density variations. Liquids and gases flowing at low speed will behave incompressible, and there will not be any linkage between the energy equation, the mass conservation and the momentum equations. The flow field can be solved by only considering conservation of mass and momentum equations [2].

The RANS equation for incompressible flow, with conservation of momentum through averaging the Navier-Stokes equation and the continuity conservation, and removing of the gravity and

5

temperature term, becomes in x, y and z-direction:

$$div(UU) = -\frac{1}{\rho}\frac{\partial P}{\partial x} + v \ div(grad \ U) + \frac{1}{\rho}\left[\frac{\partial(-\rho\overline{u'^2})}{\partial x} + \frac{\partial(-\rho\overline{u'v'})}{\partial y} + \frac{\partial(-\rho\overline{u'w'})}{\partial z}\right] \quad (4)$$

$$div(VU) = -\frac{1}{\rho}\frac{\partial P}{\partial y} + v \ div(grad \ V) + \frac{1}{\rho}\left[\frac{\partial(-\rho\overline{u'v'})}{\partial x} + \frac{\partial(-\rho\overline{v'^2})}{\partial y} + \frac{\partial(-\rho\overline{u'w'})}{\partial z}\right] \quad (5)$$

$$div(WU) = -\frac{1}{\rho}\frac{\partial P}{\partial z} + v \ div(grad \ W) + \frac{1}{\rho}\left[\frac{\partial(-\rho\overline{u'w'})}{\partial x} + \frac{\partial(-\rho\overline{v'w'})}{\partial y} + \frac{\partial(-\rho\overline{w'^2})}{\partial z}\right] \quad (6)$$

Since this is a steady-case simulation, the Semi-Implicit Method for Pressure Linked Equations (SIMPLE) algorithm is without the time dependent term. Due to gravity exclusion in this case the buoyant Boussinesq source term is eliminated. The high flow velocity will make the effect of buoyancy irrelevant.

The normal Reynold stresses are shown in equation 7, while the shear Reynold stresses are in equation 8:

$$\tau_{xx} = -\rho\overline{u'^2} \qquad \tau_{yy} = -\rho\overline{v'^2} \qquad \tau_{zz} = -\rho\overline{w'^2} \quad (7)$$

$$\tau_{xy} = \tau_{yx} = -\rho\overline{u'v'} \qquad \tau_{xz} = \tau_{zx} = -\rho\overline{u'w'} \qquad \tau_{yz} = \tau_{zy} = -\rho\overline{v'w'} \quad (8)$$

While equations 7 contain squared velocity fluctuations the equations 8 contain second hlmoments with association to different velocity components. For that reason, they are always non-zero and usually very large compared to the viscous stresses in a turbulence flow.

The Boussinesq eddy viscosity assumption takes into account the increase in turbulence with proportional increase in the mean rate of deformation as mentioned in section 2. The Reynold stresses in the RANS equations become:

$$\tau_{ij} = -\rho\overline{u_i'u_j'} = \mu_t\left(\frac{\partial U_i}{\partial x_j} + \frac{\partial U_j}{\partial x_i}\right) - \frac{2}{3}\rho k\delta_{ij} = 2\mu_t S_{ij} - \frac{2}{3}\rho k\delta_{ij} \quad (9)$$

where i or j=1 corresponds to the x-direction, i or j=2 the y-direction and i or j=3 the z-direction. Whilst for the Kronecker delta, δ_{ij}=1 if i=j, and δ_{ij}=0 if i $\neq$ j

Equation 9 has the mean flow straining field as:

$$-\rho\overline{u_i'u_j'} = 2\mu_t S_{ij} - \frac{2}{3}\rho k\delta_{ij} \quad (10)$$

where μ_t is the coefficient termed turbulence "viscosity" (also called the eddy viscosity). S_{ij} is the

mean strain rate and k is the mean turbulent kinetic energy, both shown in equations 11 and 12, respectively.

$$S_{ij} = \frac{1}{2}\left[\frac{\partial U_i}{\partial x_j} + \frac{\partial U_j}{\partial x_i}\right] - \frac{1}{3}\frac{\partial U_k}{\partial x_k}\delta_{ij} \tag{11}$$

$$k = \frac{1}{2}(\overline{u_1 u_1} + \overline{u_2 u_2} + \overline{u_3 u_3}) \tag{12}$$

The extra term $\frac{2}{3}\rho k \delta_{ij}$ in equation 10 is included for modelling incompressible flow to ensure that the definition of turbulence kinetic energy upholds.

3.1 The k - ϵ model

In this two-equation model as mentioned in section 2, the turbulent kinetic energy, k, and the turbulent dissipation, ϵ, are included in order to solve the turbulent viscosity, v_t. This standard k-ϵ model is from Launder and Spalding, 1974 [5].

The governing equation for turbulent kinetic energy k becomes:

$$\frac{\partial(\rho k)}{\partial t} + \partial(\rho k U) = div\left(-\overline{\rho' \mathbf{u'}} + 2\mu\overline{\mathbf{u'}s'_{ij}} - \rho\frac{1}{2}\overline{u'_i \cdot u'_i u'_j}\right) - 2\mu\overline{s'_{ij} \cdot s'_{ij}} - \rho\overline{u'_i u'_j} \cdot S_{ij} \tag{13}$$

The velocity scale, ϑ, and the length scale, ℓ, are defined by the use of k and ϵ:

$$\vartheta = k^{1/2} \qquad \ell = \frac{k^{3/2}}{\epsilon} \tag{14}$$

The two equations 14 are again used to obtain the eddy viscosity:

$$\mu_t = C\rho\vartheta\ell = \rho C_\mu \frac{k^2}{\epsilon} \tag{15}$$

The k-ϵ model uses the following transport equations for solving k and ϵ:

$$\frac{\partial(\rho k)}{\partial t} + div(\rho k \mathbf{U}) = div\left[\frac{\mu_t}{\sigma_k}grad\ k\right] + 2\mu_t S_{ij} \cdot S_{ij} - \rho\epsilon \tag{16}$$

$$\frac{\partial(\rho \epsilon)}{\partial t} + div(\rho \epsilon \mathbf{U}) = div\left[\frac{\mu_t}{\sigma_\epsilon}grad\ \epsilon\right] + C_{1\epsilon}\frac{\epsilon}{k}2\mu_t S_{ij} \cdot S_{ij} - C_{2\epsilon}\rho\frac{\epsilon^2}{k} \tag{17}$$

Since this is a steady state case the time dependent part is removed from equations 16 and 17.

The experimental constants in equations 16 and 17 are shown in Table 1:

Table 1: The experimental constants

$C_\mu = 0.09$	$C_{1\epsilon} = 1.44$	$C_{2\epsilon} = 1.92$	$\sigma_k = 1.00$	$\sigma_\epsilon = 1.30$

3.2 The k - ω model

As shown by Wilcox [6]–[9], the k-ω model can in this case be represented as the following:

The Wilcox k-ω model uses the turbulent frequency:

$$\omega = \frac{\epsilon}{k} \tag{18}$$

This will change the length scale from equation 14 in the k-ω model to:

$$\ell = \frac{\sqrt{k}}{\omega} \tag{19}$$

The eddy viscosity for the Wilcox k-ω is then:

$$\mu_t = \rho\frac{k}{\omega} \tag{20}$$

The k-ω model uses the following transport equations for solving k and ω:

$$\frac{\partial(\rho k)}{\partial t} + div(\rho k\mathbf{U}) = div\left[\left(\mu + \frac{\mu_t}{\sigma_k}\right)grad\ k\right] + P_k - \beta^*\rho k\omega \tag{21}$$

where the rate of production of kinetic energy is:

$$P_k = 2\mu_t S_{ij} \cdot S_{ij} - \frac{2}{3}\rho k\frac{\partial U_i}{\partial x_j}\delta_{ij} \tag{22}$$

$$\frac{\partial(\rho\omega)}{\partial t} + div(\rho\omega\mathbf{U}) = div\left[\left(\mu + \frac{\mu_t}{\sigma_\omega}\right)grad\ \omega\right] + \gamma_1(2\rho S_{ij} \cdot S_{ij} - \frac{2}{3}\rho\omega\frac{\partial U_i}{\partial x_j}\delta_{ij}) - \beta_1\rho\omega^2 \tag{23}$$

The experimental model constants in equations 21 and 23 are shown in Table 2:

Table 2: The Wilcox k-ω constants

$\beta_1 = 0.075$	$\beta^* = 0.09$	$\gamma_1 = 0.553$	$\sigma_k = 2.0$	$\sigma_\omega = 2.00$

3.3 The SST k - ω model

As mentioned in section 2, the SST $k - \omega$ model was proposed by Menter [10]–[14] starting in 1992. The Reynolds stress computation with the Boussinesq relationship, is the same as for k - ϵ and k - ω models. The kinetic transport equation for Menters SST k - ω model is the same as for the Wilcox original k - ω model. By substituting $\epsilon = k\omega$, the ω transport equation receives an extra source term, the cross diffusion term, compared to the Wilcox k - ω model.

If C_1 is a value for the original k - ω model and C_2 is for the Menter's k - ω model, then the transition with the blending function can be written:

$$C = F_c C_1 + (1 - F_c)C_2 \tag{24}$$

where a typical blending function is as follows:

$$F_c = F_c(\frac{\ell_1}{y}, Re_y) \tag{25}$$

were the ratio of turbulence, $\ell_t = \frac{\sqrt{K}}{\omega}$, y is the distance to the wall and the turbulence Reynolds number, $Re_y = y^2\frac{\omega}{v}$.

The limiters for the Menter SST kinetic transport equations are:

$$\mu_t = \frac{a_1\rho k}{max(a_1\omega, SF_2)} \tag{26}$$

where $S = \sqrt{2S_{ij}S_{ij}}$, $a_1 = $ constant and F_2 is a blending function:

$$F_2 = tanh\left[\left[max\left(\frac{2\sqrt{k}}{\beta^*\omega y}, \frac{500\nu}{y^2\omega}\right)\right]^2\right] \tag{27}$$

Rate of production of kinetic energy:

$$P_k = min\left(10\beta^*\rho k\omega, 2\mu_t S_{ij} - \frac{2}{3}\rho k\frac{\partial U_i}{\partial x_j}\delta_{ij}\right) \tag{28}$$

The Menter SST k-ω transport equation is:

$$\frac{\partial(\rho\omega)}{\partial t} + div(\rho\omega\mathbf{U}) = div\left[\left(\mu + \frac{\mu_t}{\sigma_{\omega,t}}\right)grad(\omega)\right] + \gamma_2\left(2\rho S_{ij} \cdot S_{ij} - \frac{2}{3}\rho\omega\frac{\partial U_i}{\partial x_j}\delta_{ij}\right)$$
$$-\beta_2\rho\omega^2 + 2\frac{\rho}{\sigma_{\omega,2}\omega}\frac{\partial k}{\partial x_k}\frac{\partial\omega}{\partial x_k} \tag{29}$$

Table 3: The Menter SST k-ω constants

$\alpha_1 = \frac{5}{9}$	$\beta_2 = 0.083$	$\beta^* = 0.09$	$\gamma_2 = 0.44$	$\sigma_k = 1.0$	$\sigma_{\omega 1} = 2.0$	$\sigma_{\omega 2} = 1.17$

4 Computational setup

The OpenFoam software solution is used for meshing and simulation. The Menter SST k-ω turbulent model is chosen for the RANS simulation. For the post-processing, Paraview has been used.

4.1 T-junction geometry

The geometry of the T-junction is pictured in Fig.1. The main pipe has an inlet on the left side and an outlet on the right side. The branch pipe on the top works as a second inlet in section 5 and as a second outlet in section 6.

4.2 Choice of solver

PotentialFoam solver solves the velocity potential, which calculates the initial velocity vectors for the inlets using 1/7 power law formulation.

The SIMPLE algorithm is a numerical method to solve Navier Stokes equations. It uses a "guess-and-correct" approach where it starts with a guessed pressure field p*. To find the velocity components, u* and v*, it discretizes the momentum equations. Afterward it solves the pressure correction p' to find the pressure and velocity. The iterations continue until convergence, until the pressure and velocity corrections reach their designated minimums. In other words, when the previously guessed values are approximately the same as the new calculated values, p*=p, u*=u and v*=v.

Geometric Algebraic Multi-Grid (GAMG) solver is a linear equation solver. The GAMG solver generates a quick solution on a mesh with a smaller number of cells. This initial guess is mapped onto a finer mesh to resolve an accurate solution of the fine mesh. This solver can be a faster method when the speed by solving first on coarser meshes outwins the speed it takes to refine the
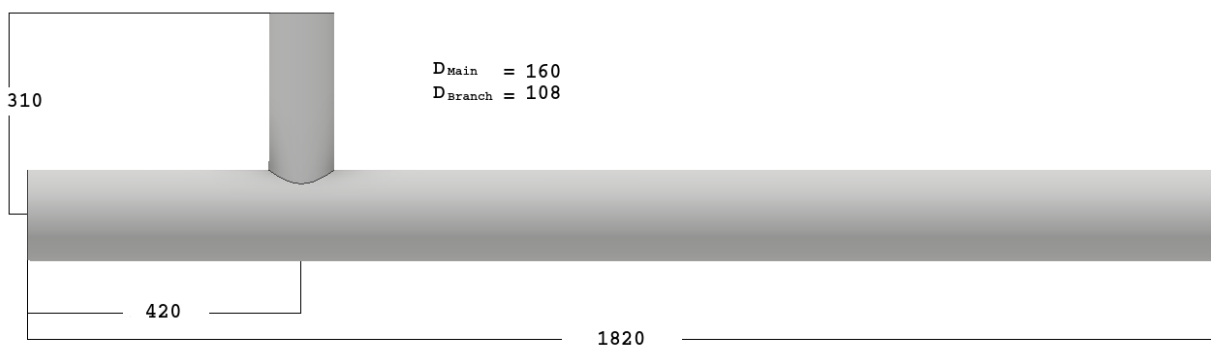

Figure 1: T-junction geometry

mesh and then the mapping of field data onto it. The user can specify the number of cells which gives a mesh size that the GAMG coarsens/refines in stages. [15]

4.3   Computational mesh

There are several different cell types:

- Triangle

- Pyramid

- Tetrahedon

- Quadrilateral

- Prism or wedge

- Hexahedron

- Polyhedron

In these T-junction both tetrahedral and snappyhexmesh have been used, based on tetrahedons or hexahedron respectively. Snappyhexmesh seems to be the most commonly used.

The collection of cells within the domain makes up the mesh or grid. In complex simulations and/or geometries the mesh generation will have a big impact on the accuracy of the results, computational time and rate of convergence. A fine grid will almost always deliver better results than a coarser grid with fewer cells. Up to a certain point this will be true, but there will be a limit for the measurable resolution of significant numbers. After this point the reliability of the extra precision will diminish. For simple geometries like the T-junction, hexahedron meshes can provide high-quality solutions with fewer cells than a comparable tetrahedon mesh. Local refinement of the mesh on areas with large flow changes or of particular importance would also balance accuracy of results with computational time and resources. Adding layers near surfaces will help capture the no-slip condition more accurately. Sharp corners where the branch pipe is connected to the main pipe, would be another problem area on the T-junction. From Fig.2 one can see that the mesh layers near the sharp corners of the intersection might cause significant inaccuracy in flow simulation in this region.

To illustrate the importance of the mesh a grid study has been done where the amount of initials cells were reduced by about 30%, with and without layers, three times.

The layer settings are listed in table 4.

Table 4: Layer settings of the mesh

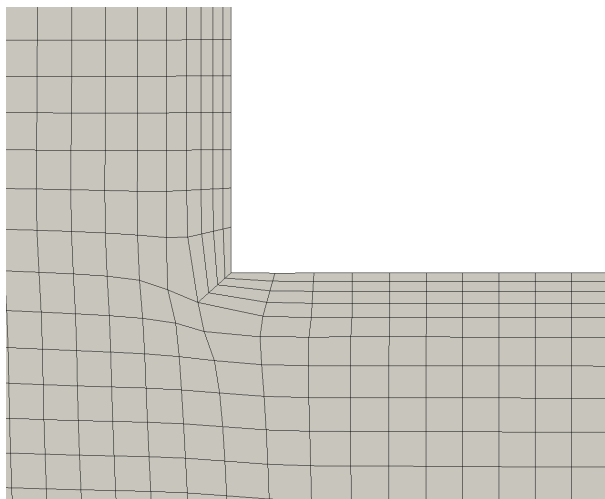|	
Numbers of surface layers	4
Final layers thickness	0.4
Expansion ratio	1.2

Figure 2: Grid of the corner of the T-junction

The tables 5 to 8 show the details of the different meshes used in the simulations. The first case was done with the initial cell amount 757x127x215 in x, y and z-direction respectively, which gives 20 669 885 cells before the snappyhexmesh. Table 5 shows that the number of cells are reduced to 2 016 979. The next case was done with about 30% reduction of the total number of cells before running. The following two cases were done with about 60% and 90% reduction. The other mesh parameters remained the same.

From table 5 the worst skewness is as high as 12.8998. This is above the setting in the meshQualityControls dictionary where the maxInternalSkewness is set to four. The high skewness number might be expected to lead to computational problems, but with further examination of the full grid, the skewness shows to be of less importance than initially believed. The skewness is placed all the way to the right and left end of the main pipe as shown in Fig. 3 and 4. For a better visualization, Fig. 4 shows a close up. However, the main focus here is at the intersection of the pipes, so the skewness will only play an insignificant role, if at all.

4.4   Initial boundary conditions

In the case setup some assumptions have been made:

Table 5: Mesh parameters for full grid size

	With layers	Without layers
Numbers of cells	2 016 979	1 585 645
Hexahedra	1 966 568	1 536 639
Prisms	48 870	48 776
Tet wedges	4	4
Polyhedra	1 537	226
Worst skewness	12.89977709	2.215688068

Table 6: Mesh parameters with 30% reduction in cell numbers

	With layers	Without layers
Numbers of cells	755 713	545 393
Hexahedra	730 788	521 250
Prisms	24 041	24 041
Tet wedges	6	6
Polyhedra	878	96
Worst skewness	2.33943124	1.481343576

Table 7: Mesh parameters with 60% reduction in cell numbers

	With layers	Without layers
Numbers of cells	170 025	101 645
Hexahedra	162 073	94 015
Prisms	7 586	7 582
Tet wedges	4	4
Polyhedra	362	44
Worst skewness	2.197887458	1.89863878

Table 8: Mesh parameters with 90% reduction in cell numbers

	With layers	Without layers
Numbers of cells	4 754	1 518
Hexahedra	4 086	957
Prisms	568	550
Tet wedges	4	3
Tetrahedra	0	1
Polyhedra	96	7
Worst skewness	1.369532586	8.072
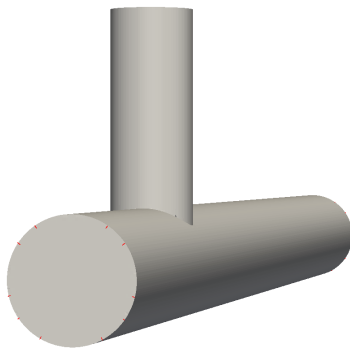
(a) Skewness on left side of the T-junction
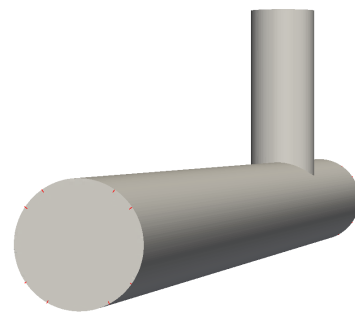
(b) Skewness on right side of the T-junction

Figure 3: Skewness on the T-junction

(a) Cross section
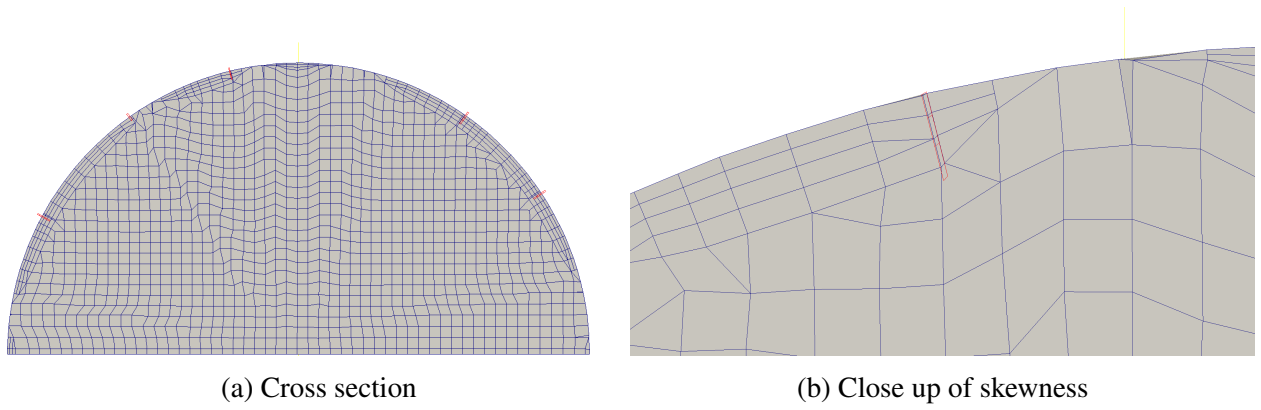
(b) Close up of skewness

Figure 4: Skewness on the grid

- fully developed flow at inlets

- the flow is following a 1/7 power law (turbulent flow)

- constant fluid properties

- steady & incompressible fluid

- zero pressure at the outlet

The fluid properties of water are listed in table 9.

Usually turbulence occurs at Reynolds numbers above 10^2, but in the special case of pipes the Reynolds number has to be above 2300 [2]. This indication of flow turbulence gives a ratio between inertial forces and viscous forces as shown in equation 30:

$$Re = \frac{\rho \cdot U \cdot D_p}{\mu}$$

(30)

where ρ is density, μ is the dynamic viscosity, U is fluid velocity and D_p is pipe diameter.

Equation 31 gives the turbulence intensity at the core for a fully developed pipe flow.

$$I = 0.16 \cdot Re^{-\frac{1}{8}}$$

(31)

By the use of turbulence intensity, I, and flow velocity, U, one derives turbulent kinetic energy, k, in equation 32.

$$k = \frac{2}{3}(U \cdot I)^2$$

(32)

Table 9: Fluid properties

	Density $[Kg/m^2]$	Dynamic viscosity $[Pa \cdot s]$
Water	998.2	0.001002

The turbulent dissipation rate, ϵ, is given by equation 33.

$$\epsilon = C_\mu^{\frac{3}{4}} \cdot \frac{k^{\frac{3}{2}}}{l} \tag{33}$$

where the turbulent model constant, C_μ can be found in table 1, and the turbulent length scale is as follows, $l = 0.07 \cdot D_p$. The turbulent length scale describes the size of eddies in a turbulent flow and the D_p is the pipe diameter.

The specific turbulent dissipation rate, ω, in equation 34, uses the same turbulent model constant, C_μ, as in equation 33.

$$\omega = C_\mu^{-\frac{1}{4}} \ \frac{\sqrt{k}}{l} \tag{34}$$

The assumption of fully developed flow in the inlets are not quite accurate but very close, as Fig.5 shows. Due to the non-slip conditions along the wall there is no velocity there, and the velocity increases almost parabolic towards the middle, as in a fully developed flow. From Fig.1 the diameter on the inlets are $D_{inlet1} = 140$ and $D_{inlet2} = 100$, which corresponds with the x-axis in Fig.5. That is the reason the graph for inlet 2 goes more to the right than for inlet 1. In a fully developed laminar flow in a pipe, the flow follows a parabolic curve. Since this is turbulence flow, the flow profile becomes flatter in shape. This fabricated flow profile is made by the use of 1/7 power law. In general this gives a good description of a fully developed turbulent flow, even though the shape deviates at the middle by having a too sharp tip.

1/7 Power law:

$$u = u_0(1 - \frac{r}{R})^{\frac{1}{7}} \tag{35}$$

To show the velocity profile close to the cross section, Fig. 7 illustrates the velocity taken at position 1D as depicted in fig. 6. The position is the distance 1D, where the diameter of the main pipe is used, from the middle of the cross section in each pipe.
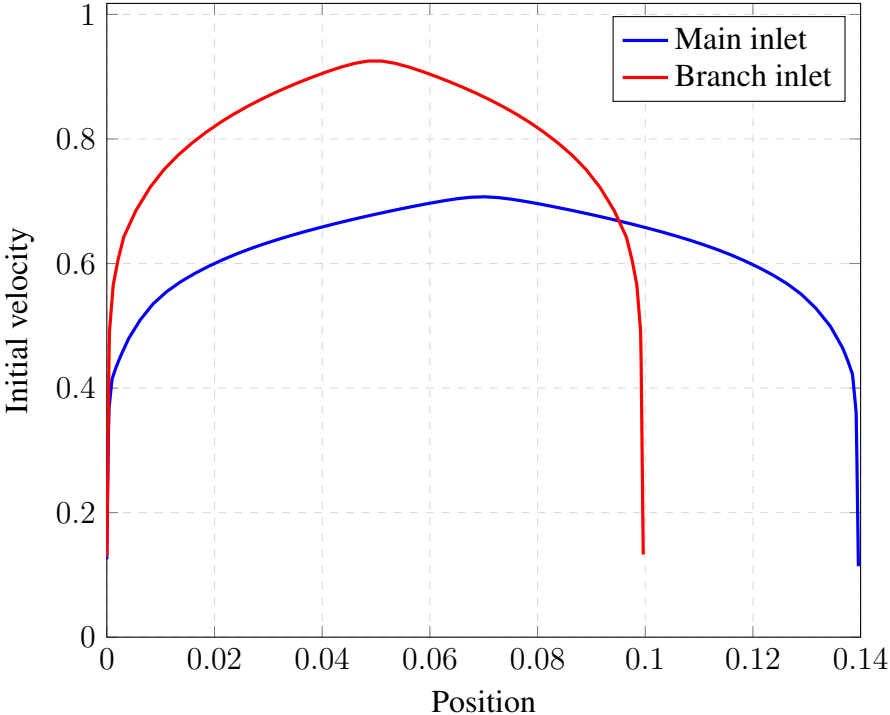
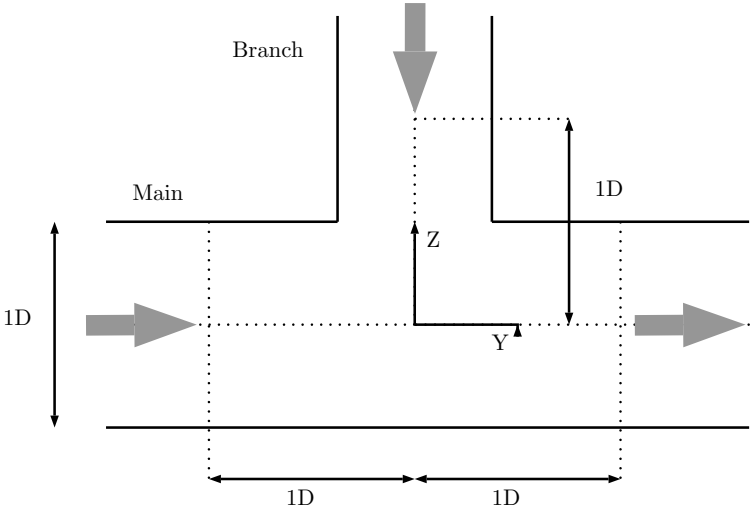Figure 5: Initial velocity for main and branch inlet

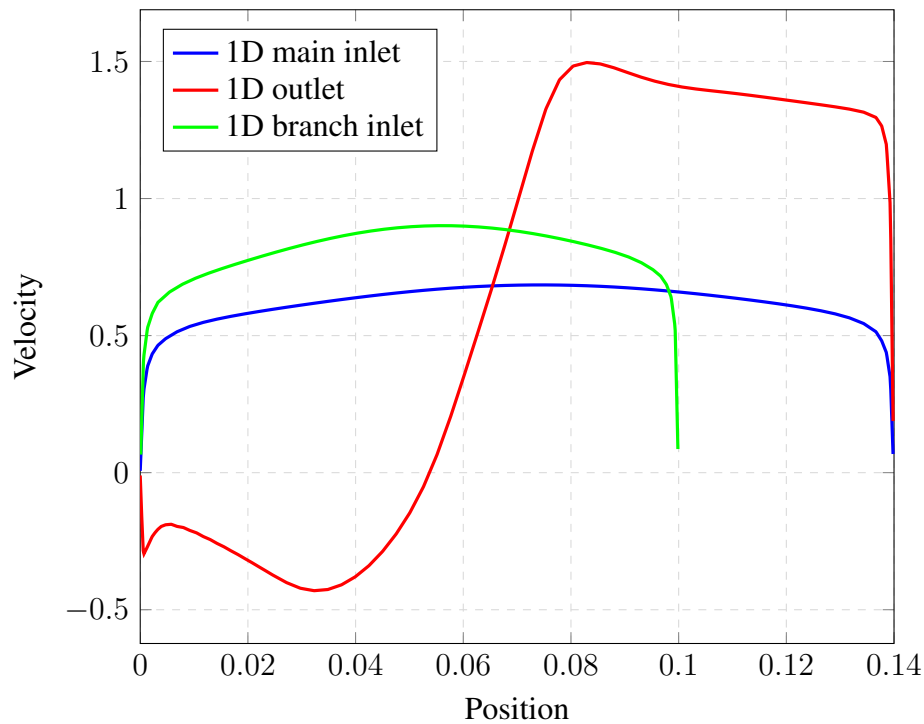Figure 6: Cross section of t-junction I

Figure 7: Velocities at 1D

5 T-junction I

5.1 Introduction

Since the T-junction is a well documented subject, especially the case where there are two inlets and one outlet, the CFD simulations are employed. This will be a validation case since experiments have already been performed on this situation.

The geometry of this T-junction is shown in Fig.1, as mentioned earlier in section 4. Fig.8 shows a close up of the cross section to better illustrate the flow directions in the inlets and the outlet. The main inlet is on the left end of the main pipe, the branch inlet is on the top and goes downwards, and the outlet is on the right end of the main pipe.

5.2 Initial boundary condition

The initial conditions for T-junction I are listed in table 10.

Table 10: Initial conditions for T-junction I

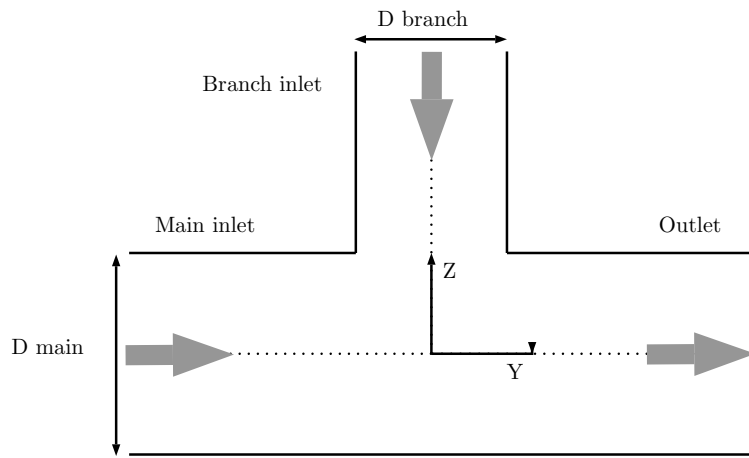| Property	Re	u_0
Main pipe	$99.84 x 10^3$	0.716
Branch pipe	$93.13 x 10^3$	0.935

Figure 8: Cross section of t-junction I

Table 11: Boundary conditions for T-junction I

Surface domain	Inlet, main	Inlet, branch	Outlet	Pipe/Wall
Patch type	Patch	Patch	Patch	Wall
Pressure, P	zeroGradient	zeroGradient	fixedValue	zeroGradient
Velocity, U	codedFixedValue	codedFixedValue	zeroGradient	noSlip
Epsilon, ϵ	turbulentMixing LengthDissipation RateInlet	turbulentMixing LengthDissipation RateInlet	zeroGradient	epsilon WallFunction
k	turbulentIntensity KineticEnergyInlet	turbulentIntensity Kinetic EnergyInlet	zeroGradient	kqRWall Function
nut	calculated	calculated	zeroGradient	nutUSpalding WallFunction
ω	turbulentMixing LengthFrequency Inlet	turbulentMixing LengthFrequency Inlet	zeroGradient	omegaWall Function

6   T-junction II

6.1   Introduction

In this part there will be focus on a T-junction with flow out of the branch pipe. In most cases there are two inlets and one outlet as in section 5. In this section the previous inlet in the branch pipe will now be an extra outlet. So there will be one inlet flow and two outlet flows, one of them a branch outlet and the other a main outlet. The configuration of the flow directions is illustrated in Fig.9. Almost all others parameters will be the same as in the previous section, T-junction I. The difference in the settings between the two cases are listed in the initial boundary conditions, in table 12 and 13.

In section 5 the T-junction had two inlets and one outlet. There exist several papers on this configuration. When it comes to this configuration, but when it comes to a configuration where there is flow out of the branch pipe, there is sparse documentation.

Due to the lack of information on this latter configuration, the geometry has been changed to match cases where there are some experimental data. Hopefully this will strengthen the credibility of the choice of models and solvers.

In this section there are three different configurations of flows out of the branch:

- T-junction IIa: has one inlet and one outlet

- T-junction IIb: has one inlet and two outlets, main and branch

    T-junction IIb(i): Flow rate 0.6:0.4

    T-junction IIb(ii):Flow rate 0.8:0.2

- T-junction IIc: has one inlet and equal flow rate for the main and branch

The geometry for T-junction IIa is the same as for T-junction I in Fig.1. For the case T-junction IIb, Beneš et al. in 2013[16], did a numerical simulation of a T-junction. To compare the few PIV measurements in the paper, a similar model was created with the same solvers and settings as previously mentioned in this paper, only with a slight change in the geometry. The overall diameter was set to 100mm and the Re=30 000. The geometry of the model is shown in Fig.10

For the case T-junction IIc, Sierra-Espinosa et al.[17], [18] investigated a water flow out of the branch in a T-junction numerically and experimentally. The represented data are mean velocity by the use of Laser Doppler Anemometer (LDA). The branch exit flow rate was set to be 50% of the inlet flow rate. The overall pipe diameter, D = 50 mm, and the $Re = 1.26x10^5$. Sierra-Espinosa had a smooth chamfer, of radius r = 0.25D, which is important, considering that the numerical experiment in this case has a sharp edge. This will increase the severity of the swirling motion [19]. All other settings are the same as for T-junction II. The illustration of the geometry of the
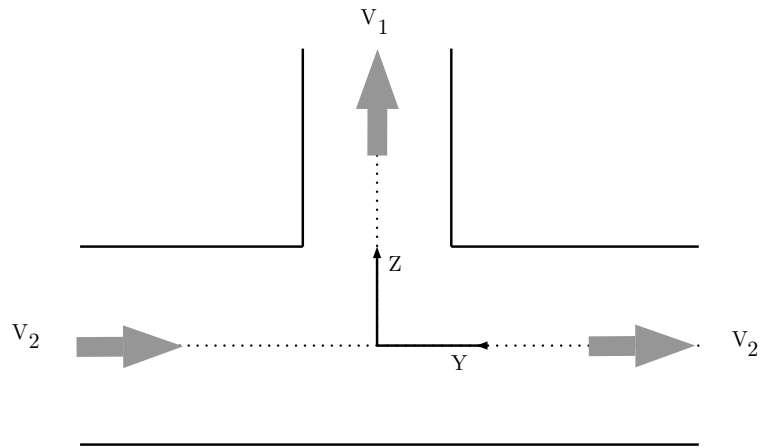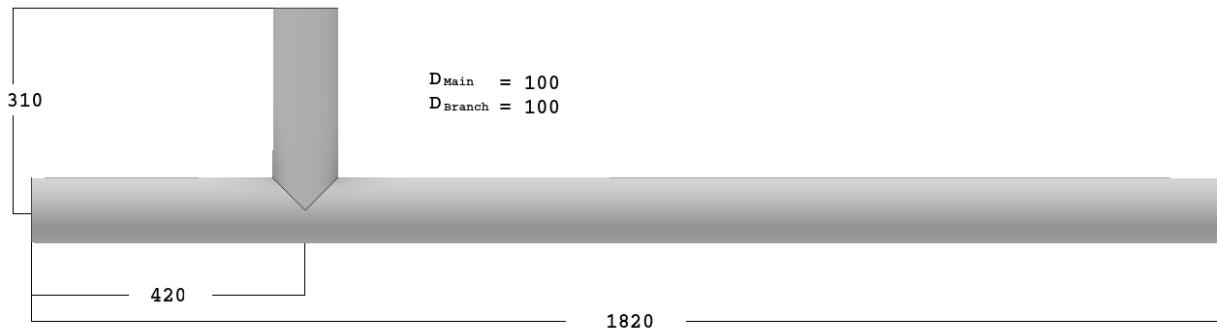
Figure 9: Cross section of t-junction II
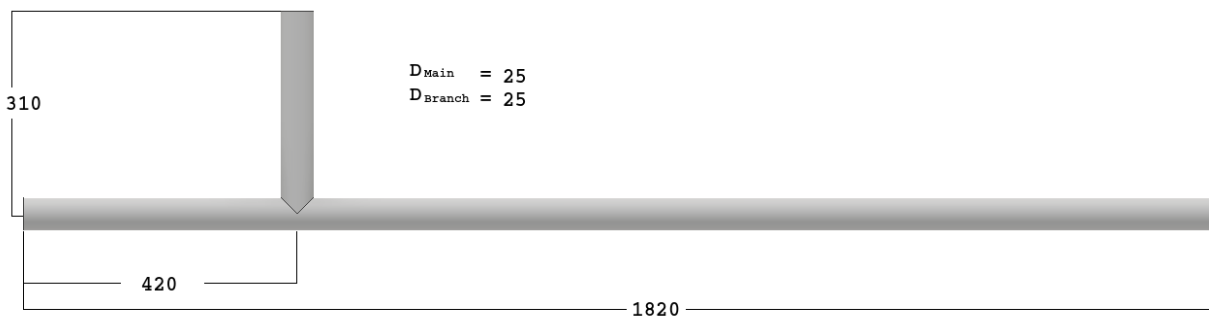

Figure 10: Geometry of T-Junction IIb

Figure 11: Geometry of T-Junction IIc

T-junction IIc is in Fig.11

6.2   Initial boundary conditions

Table 12: Initial conditions for T-junction IIa

Property	Re	u_0
Main pipe	$99.84x10^3$	0.716

Table 13: Boundary conditions for T-junction IIa

Surface domain	Inlet	Outlet, branch	Outlet, main	Pipe/Wall
Patch type	Patch	Patch	Patch	Wall
Pressure, P	zeroGradient	zeroGradient	fixedValue	zeroGradient
Velocity, U	codedFixedValue	flowRate OutletVelocity	flowRate OutletVelocity	noSlip
Epsilon, ϵ	turbulentMixing LengthDissipation RateInlet	zeroGradient	zeroGradient	omegaWall Function
k	turbulentIntensity KineticEnergyInlet	zeroGradient	zeroGradient	kqRWallFunction
nut	calculated	zeroGradient	zeroGradient	nutUSpalding WallFunction
ω	turbulentMixing LengthFrequency Inlet	zeroGradient	zeroGradient	omegaWall Function

Table 14: Initial conditions for T-junction IIb(i)

Property	Re	u_0	Q_3/Q_1
Main pipe	$30x10^3$	0.613	0.6/0.4

Table 15: Initial conditions for T-junction IIb(ii)

Property	Re	u_0	Q_3/Q_1
Main pipe	$30x10^3$	0.613	0.8/0.2

Table 16: Boundary conditions for T-junction IIb

Surface domain	Inlet	Outlet, branch	Outlet, main	Pipe/Wall
Patch type	Patch	Patch	Patch	Wall
Pressure, P	zeroGradient	zeroGradient	fixedValue	zeroGradient
Velocity, U	codedFixedValue	flowRate OutletVelocity	flowRate OutletVelocity	noSlip
Epsilon, ϵ	turbulentMixing LengthDissipation RateInlet	zeroGradient	zeroGradient	omegaWall Function
k	turbulentIntensity KineticEnergyInlet	zeroGradient	zeroGradient	kqRWallFunction
nut	calculated	zeroGradient	zeroGradient	nutUSpalding WallFunction
ω	turbulentMixing LengthFrequency Inlet	zeroGradient	zeroGradient	omegaWall Function

Table 17: Initial conditions for T-junction IIc

Property	Re	u_0	Q_1/Q_2
Main pipe	$1.26x10^5$	2.53	0.5

Table 18: Boundary conditions for T-junction IIc

Surface domain	Inlet	Outlet, branch	Outlet, main	Pipe/Wall
Patch type	Patch	Patch	Patch	Wall
Pressure, P	zeroGradient	zeroGradient	fixedValue	zeroGradient
Velocity, U	codedFixedValue	flowRate OutletVelocity	flowRate OutletVelocity	noSlip
Epsilon, ϵ	turbulentMixing LengthDissipation RateInlet	zeroGradient	zeroGradient	omegaWall Function
k	turbulentIntensity KineticEnergyInlet	zeroGradient	zeroGradient	kqRWallFunction
nut	calculated	zeroGradient	zeroGradient	nutUSpalding WallFunction
ω	turbulentMixing LengthFrequency Inlet	zeroGradient	zeroGradient	omegaWall Function

7 T-junction III

7.1 Introduction

As mentioned in the introduction, the t-junction is a well known subject. Even though there have been written several papers on this subject few experiments have been done, which has caused several numerical simulations to be based on the same experiment [3], [20].

For this last case, which is not based any experiment, one will have to apply the data and knowledge from the two previous cases, T-junction I and T-junction II, for the piping configuration of T-junction III.

In Fig.13 the geometry of T-junction III is illustrated. There are two inlets and two outlets. It is important to minimize the mixture of the fluids to avoid too much velocity loss. Due to this configuration being both a forward and a backward flowing system, there is nothing to be gained by changing the angles of the branches. The advantage one may gain when the main flow goes in one direction will be more than offset when the flow goes in the opposite direction. If the system only had one main flow direction, the angles would be a good parameter to change in attempts to minimize energy loss. The distance between the different branches plays perhaps the most important role in this case. To take a closer look at the importance of this effect, the distance between the pipes are placed at 1.5D, 2D and 2.5D. By visualization one can see the effect the proximity the branches have on the flow. This is important in determining the optimal distance between the branch pipes. The geometry, with the different spacings between the branches, is shown in Fig.13, 14, 15 and 16. Fig.12 shows the flow pattern of the junctions.

7.1.1 Initial boundary conditions

The table 19 shows the mesh parameters in the simulations.
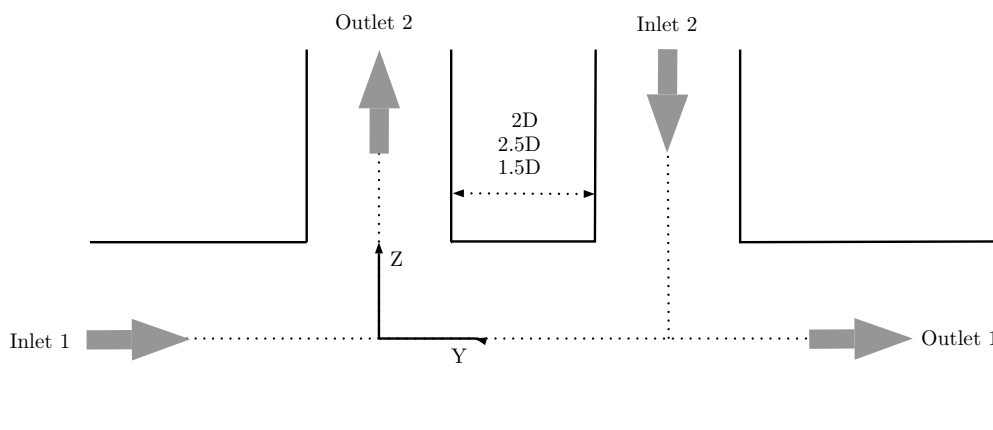
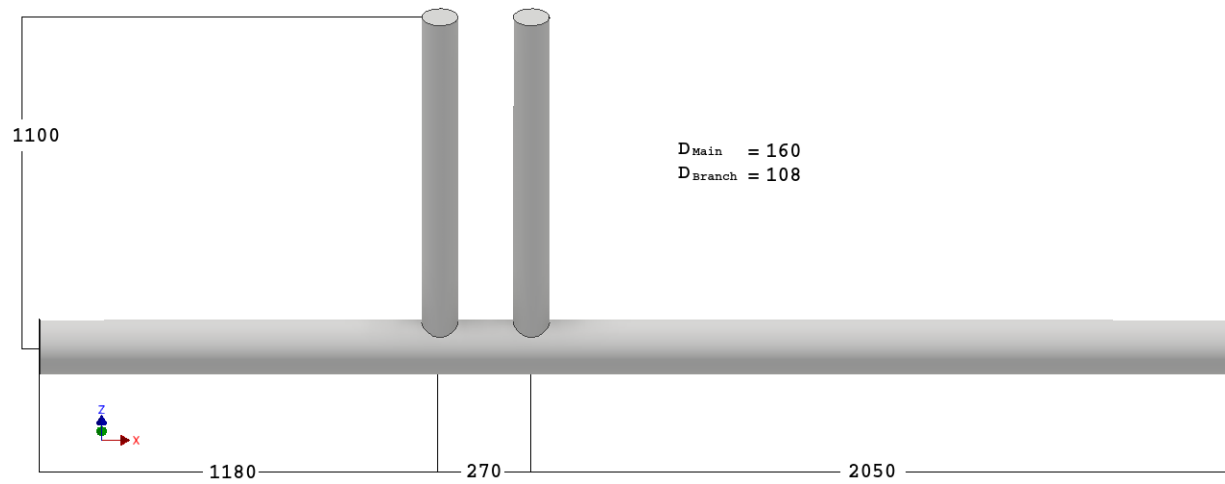Figure 12: Cross section of t-junction III
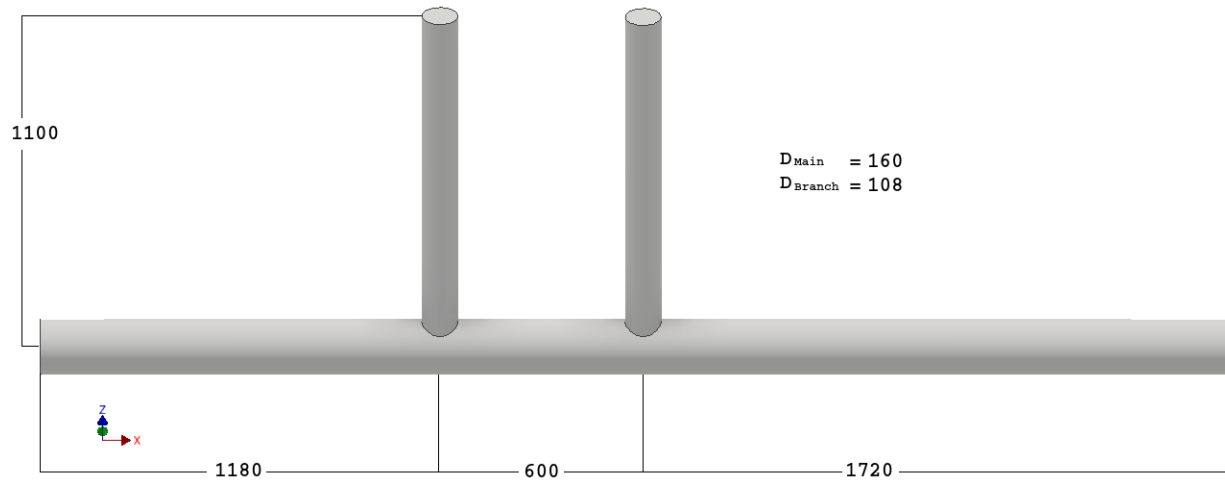
Figure 13: T-junction III

Figure 14: T-junction III 2.5D
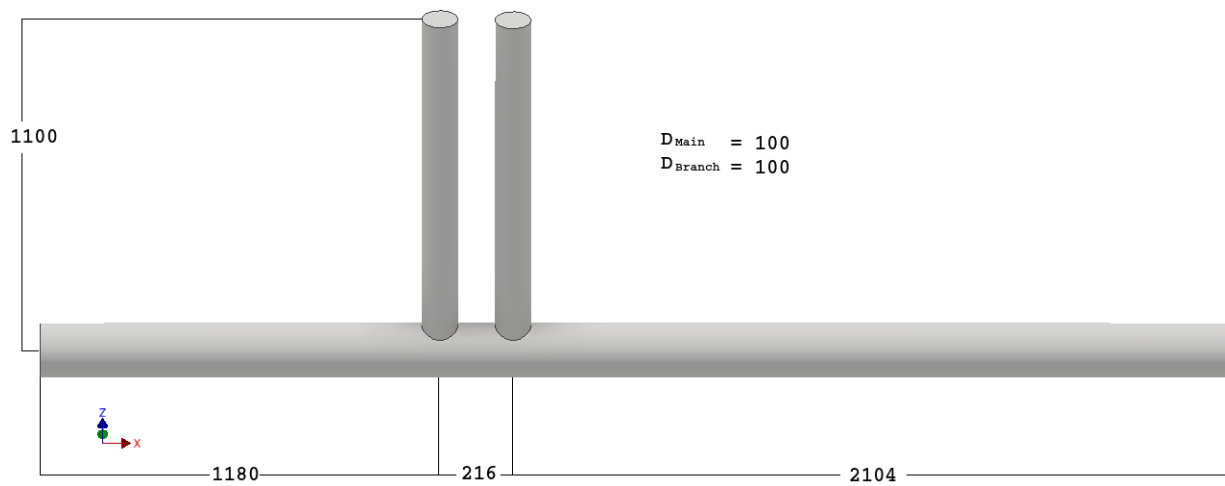
Figure 15: T-junction III 2D
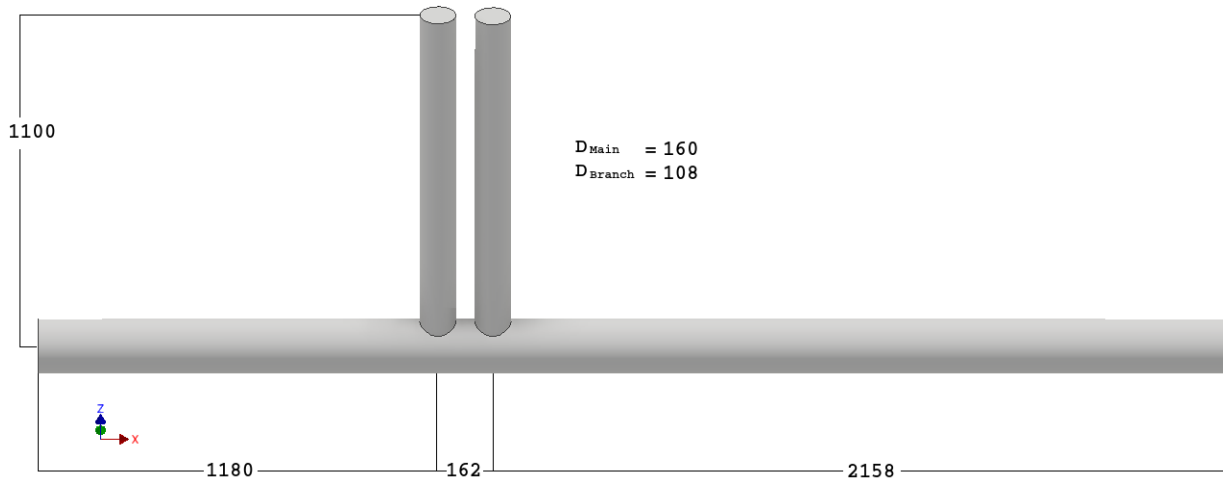
Figure 16: T-junction III 1.5D

Table 19: Mesh parameters

	Value
Numbers of cells	701 705
Hexahedra	651 547
Prisms	29 023
Tet wedges	63
Polyhedra	21 072
Worst skewness	2.694676212

Table 20: Initial conditions for T-junction III

Property	Re	u_0
Inlet 1	$814x10^3$	0.511
Inlet 2	$118x10^3$	1.1

Table 21: Boundary conditions for the hydronic system (a)

Surface domain	Inlet, main	Inlet, branch
Patch type	Patch	Patch
Pressure, P	zeroGradient	zeroGradient
Velocity, U	codedFixedValue	codedFixedValue
Epsilon, ϵ	turbulentMixing LengthDissipation RateInlet	turbulentMixing LengthDissipation RateInlet
k	turbulentIntensity KineticEnergyInlet	turbulentIntensity KineticEnergyInlet
nut	zeroGradient	zeroGradient
ω	turbulentMixing LengthFrequency Inlet	turbulentMixing LengthFrequency Inlet

Table 22: Boundary conditions for the hydronic system (b)

Surface domain	Outlet, main	Outlet, branch
Patch type	Patch	Patch
Pressure, P	fixedValue	zeroGradient
Velocity, U	zeroGradient	flowRateOutletVelocity
Epsilon, ϵ	zeroGradient	zeroGradient
k	zeroGradient	zeroGradient
nut	zeroGradient	zeroGradient
ω	zeroGradient	zeroGradient

Table 23: Boundary conditions for the hydronic system (c)

Surface domain	Pipe/Wall
Patch type	Wall
Pressure, P	zeroGradient
Velocity, U	noSlip
Epsilon, ϵ	epsilonWall Function
k	kqRWallFunction
nut	nutUSpalding WallFunction
ω	omegaWall Function

8 Results

8.1 Mesh generation results

All the results from the mesh generations in Fig.18 and 19 are taken the distance 1D from the cross section as illustrated in Fig. 17

From section 4, there were generated eight different initial mesh set-ups on T-junction I. Four of these had different initial cell numbers, there where about 30% reduction for each case, and all of these four where simulated with and without layers, so in total eight different meshes.

In Fig. 18 the difference in cell reductions with and without layers are illustrated. To get a better visualization of the grids, only the right upper quadrant of the cross section is depicted. The slice of the main pipe is taken the distance 1D from the intersection in the T-junction. On the left side are the cases with layers, while on the right side those without layers. Since layering is a separate addition to the cell numbers, this function will increase the total number of cells. So the same base number of cells with or without layers will have a different total number of cells. In the area close to the wall there will be a significant change in speed from the no-slip condition at the wall to the middle of the pipe diameter. By adding layers it will be easier to catch the changes in the flow and
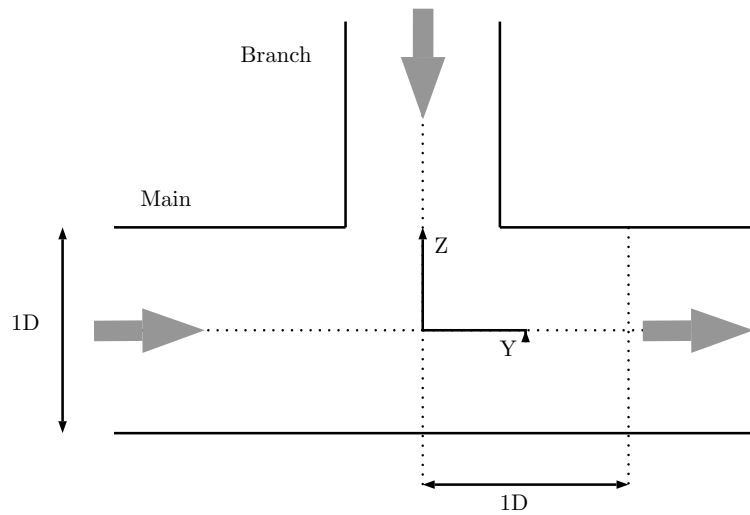
Figure 17: Cross section of t-junction I

get a smoother transition between the wall and the main flow.

For each reduction in cell numbers, there are visibly fewer cells shown. The greatest visualized difference is, unsurprisingly, between Fig.18a and Fig.18h. These two cases are also the two with the the greatest difference in cell numbers.

Fig.19 illustrates the velocity profiles of the different mesh cases illustrated in Fig.18. The placement arrangements are the same, to the left are those with layers and to the right are those without layers. All these figures have the same velocity scale that are placed to the far right side on each line. The placement of the figures are 1D from the intersection point, where the inlet flows meet, in the T-junction on the right side.

All the figures to the right in Fig.19, the figures without layers, have a thicker velocity edge, the no-slip layer is wider and more uneven, compared to those with layers. Since each cell has a value, there is no gradient in a cell, and the cells are larger in size than the layers, this will lead to a more noticeable no-slip zone. So all the cells that touch the outer boundary will have a zero velocity, no matter the thickness of the cell. Due to the cell difference in size and form the right side figures will also have a more ragged line, since this is a circumference edge and the main cells are hexahedron. With thinner cells that follow the contour of the edge the layers are better equipped to handle the transition from the no-slip condition to a higher value of velocity. The thin layering will not hold the zero velocity along the boundary for long. The column of figures on the left side in Fig.19, all have a realistic presentation of the boundary layer. The figures on the right side have a very jagged, unrealistic boundary layer. The fewer cells, the more pixelated layers the boundary gets.

Within the main flow inside the middle of the pipe, the recirculation zone holds the best evidence of the effect of decreasing the number of cells. As the numbers of cells in the grid reduces, the blurriness increases. After 90% cell reduction the figure is very pixelated. Another change in the recirculation zone is the shape of this zone. Fig.19a has a more oval shape with corners. The corners on the left and right side of the recirculation zone seem to get rounder with a decreasing cell number. On the last reduction, 90%, Fig.18h has a rounder shape than Fig.19a. The higher

amount of reduction, the rounder the recirculation zone becomes. This might be due to the reduced influence of the main inlet.

A vertical cross section of the T-junction on the xz-plane, shows the profile of the recirculation zone in Fig.20. There is a thicker no-slip layer that is quite prominent after the recirculation zone for the cases without layers. The mixing of the fluids are kept away from the no-slip area, which will lead the mixing zone to extend further down the pipe. For the case with full grid size and down to 90% mesh reduction, the recirculation zone appears to become shorter, and the average velocity close to the end of the pipe is higher. The thickness of the high velocity flow under the recirculation is much thinner for the full grid than for the 90% reduction, even though the velocity scale goes higher for the full grid case at this position. The recirculation zone in the 90% reduction case goes shallower and is more defused compared to the full mesh case.

The u_x from Fig.21a shows a slight decrease in velocity in the recirculation zone compared to the same case without layers. In Fig.21b the original case with full grid has a higher peak of velocity in the cross section and in the recirculation zone than for the case with 90% reduction in the mesh.

By reducing the mesh resolution there will be an increase in computational speed at the cost of accuracy. This can be advantageous in rough simulations of prototypes before committing to using a large amount of resources on the final computation.

8.2   T-junction I

The experimental data originates from the experiment performed by the collaboration of OECD/NEA and Vattenfall Research and Development at the Älvkarleby Laboratory in Sweden. Since this data have not been made public the experimental data have been taken indirectly, from other benchmark studies.

In Fig.22[21] the mean axial velocities over the diameter of the main pipe are illustrated. On the left side are the velocities along the horizontal diameter-line (that goes along the y-axis) at the different locations along the x-axis of the pipe. The figures on the right side are from the vertical line (that goes along the z-axis). On the y-axis on Fig.22 is the U_x velocity over the $U_{cl,x}$, and the x-axis is over the diameter of the main pipe.

Due to the momentum ratio of the branch pipe, the main flow decreases in the center and accelerates at the sides. In this way the flow through the main inlet is hindered by the flow through the branch pipe. This explains the increase in the normalized velocity at the edges (the pipe wall). In the position X/D=1.6 on the left side on Fig.22 the computational results are a very close match to the experimental data. As the distance increases further away from the cross section along the x-axis the computational results diverge from the experimental data. The normalized velocities at the edges slow down as one moves further away from the cross section. The smoothing over the velocity-line across the diameter in the experimental data is significantly quicker than for the computational data. The recirculation zone seems to extend further with the RANS model than
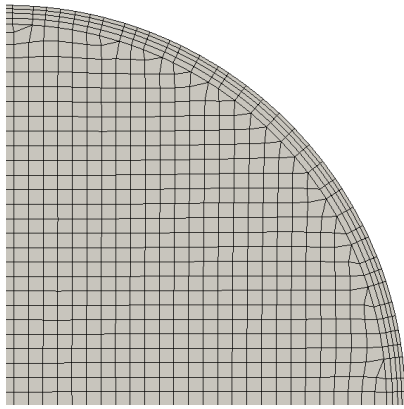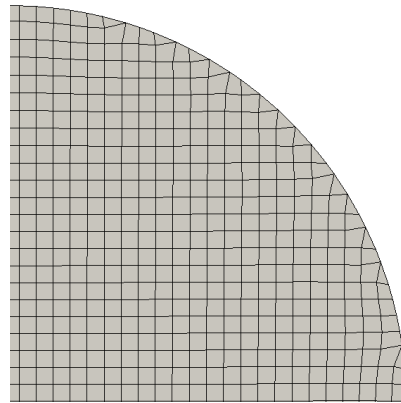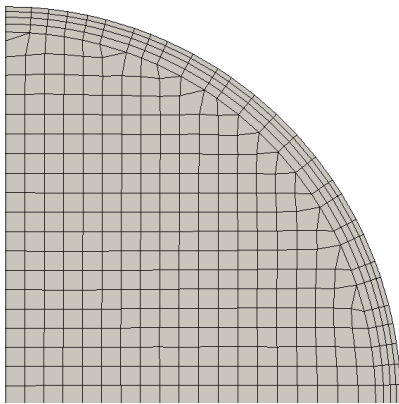
(a) Original
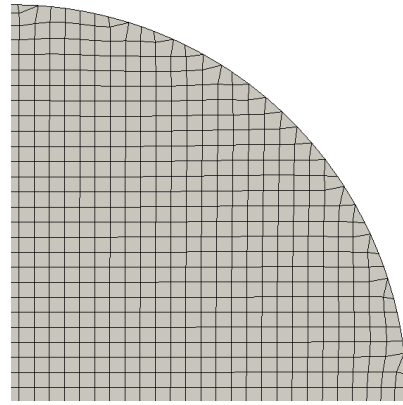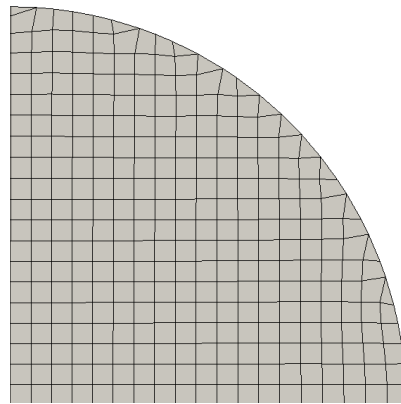
(b) Original without layers
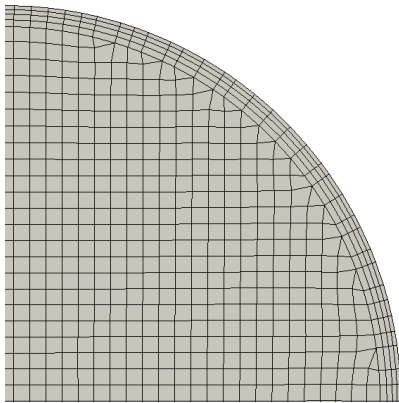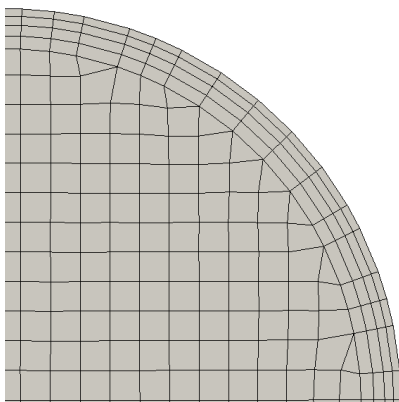
(c) 30% Reduction

(d) 30% Reduction without layers

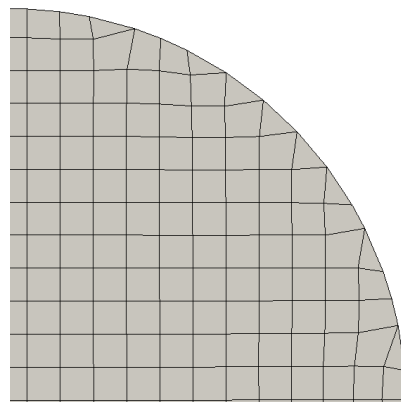(e) 60% Reduction

(f) 60% Reduction without layers

(g) 90% Reduction

(h) 90% Reduction without layers
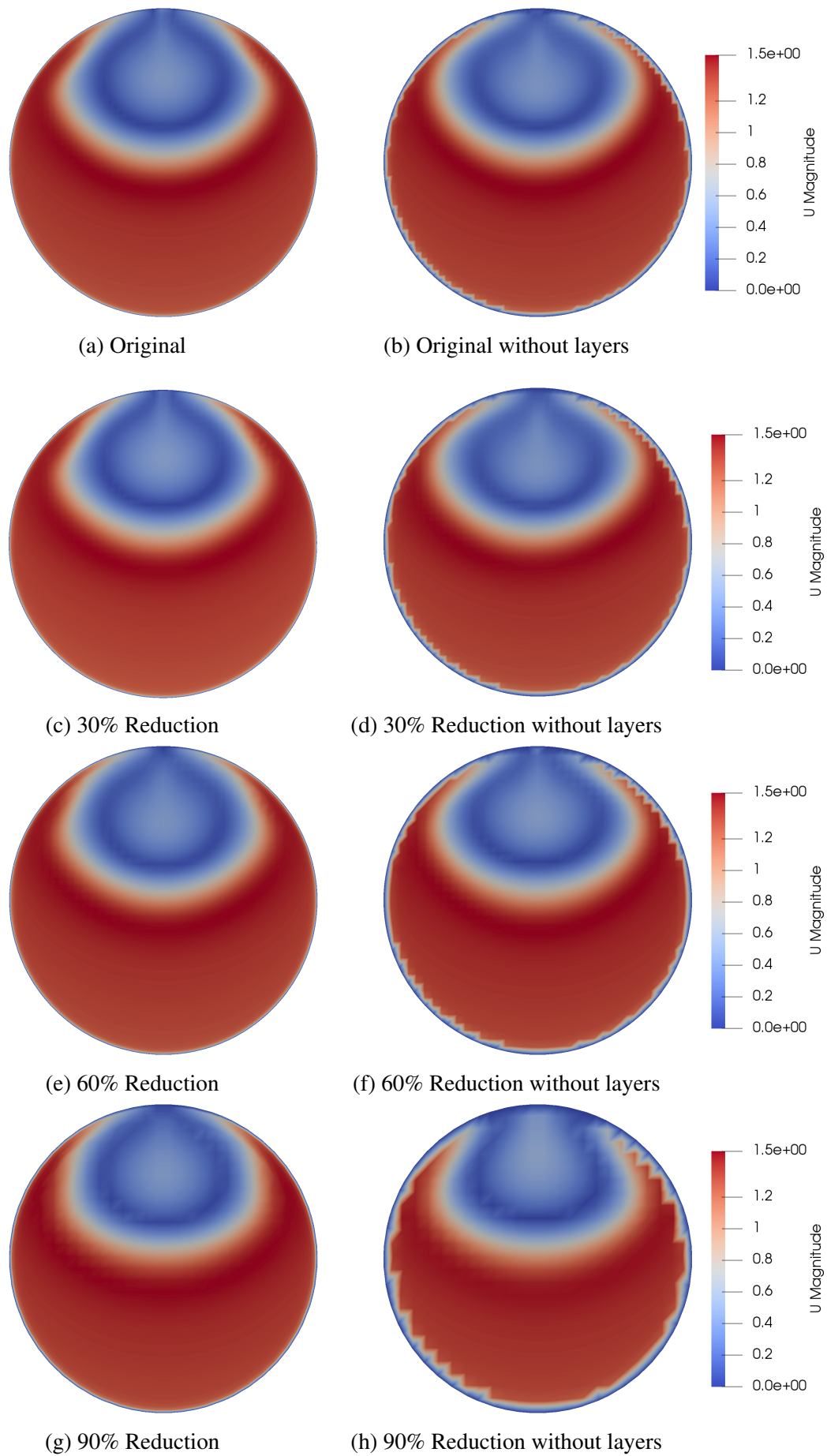
Figure 18: Generated meshes

(a) Original

(b) Original without layers

(c) 30% Reduction

(d) 30% Reduction without layers

(e) 60% Reduction

(f) 60% Reduction without layers

(g) 90% Reduction

(h) 90% Reduction without layers

Figure 19: Velocities at 1D

(a) Original

(b) Original no layers

(c) 30%Reduction

(d) 30%Reduction no layers

(e) 60%Reduction

(f) 60%Reduction no layers

(g) 90%Reduction

(h) 90%Reduction no layers
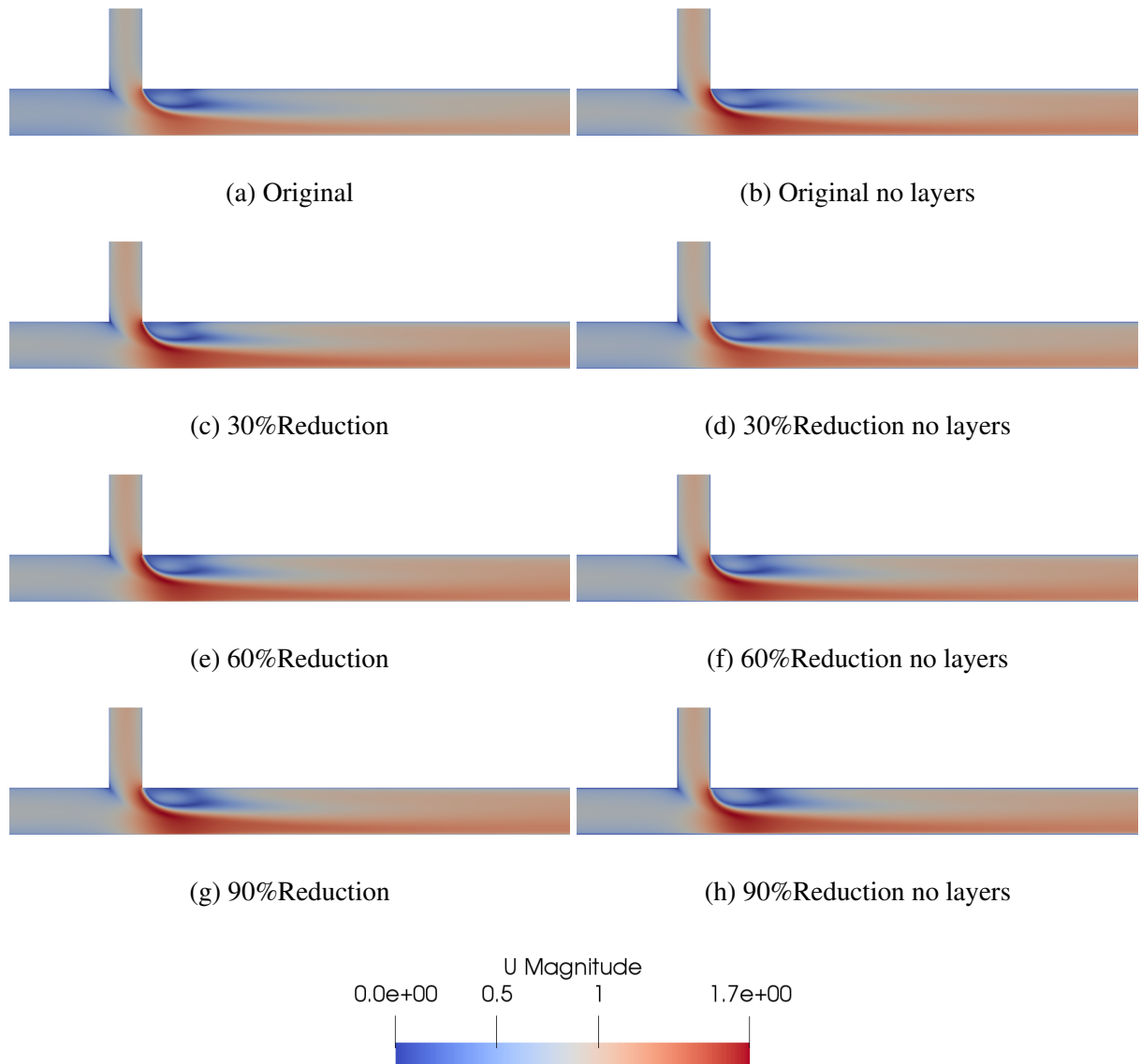
Figure 20: Cross section of velocity profile for the different grid configurations
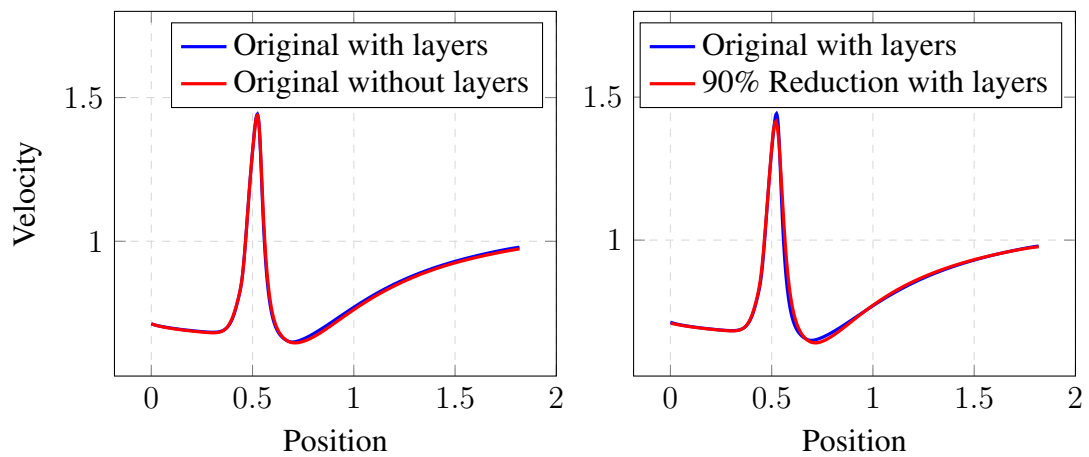
Figure 21: Comparison of u_x along the center line

from the experiment. This might be an indication that the RANS model falls somewhat short in simulating the recirculation zone.

On the right side of Fig.22, where the normalized velocity is plotted over the vertical diameter, one can see that the shapes are quite similar. There is a bit more curvature in the computational data at X/D=1.6 than for the experimental data. The velocity close to the top of the pipe, in the recirculation zone, is higher in the computational data. This zone seems to be more affected by the branch flow than in the experiment.

The mean center line velocity in Fig.23[20] shows that the computational value at the distance x/D=1.6 is higher than for the experimental value. This is the same as on the right side of Fig.22. The velocity in the recirculation zone is higher in the computation than in the experiment. As the measurements are taken further down the pipe, the different values get closer. At the positions x/D=3.6 and 4.6 the experimental and computational data are quite similar.

Overall, the RANS with the SST $k - \omega$ model, corresponds quite well with the experimental data from the Älvkarleby laboratory of Vattenfall Research and Development in Sweden. Even though LES is often preferred in the research community as in [3] and gives closer results with these experimental data in [21], the SST $k - \omega$ model gives good results considering the computational cost.

8.3   T-junction II

Fig. 25 shows the sliced T-junction IIa where there is only one inlet and one outlet. There is an increase in velocity as the fluid flows upwards in the smaller branch. As the fluid bends in the branch the velocity increases rapidly, before the recirculation zone extends outward in the diameter of the branch. In the stream tracer in Fig.26 the recirculation zone after the bend in the main pipe is more visible.

By looking at the stream tracer in the case of T-junction IIbi in Fig.29, the flow that continues along the main pipe extends quite a bit, but not all the way out of the main outlet. Since 60% of the flow is supposed to go out the main pipe this leads to this flow having a lot of vortex and turbulence, so that the magnitude of the velocity falls under the value $3.0x10^{-3}$ on the scale bar. By checking the bulk velocity out of the pipe it seems that the flow out of the branch pipe is closer to 33% than 40% which was previously believed. This indicates that there is more disturbance in the flow than initially assumed, as shown in Fig.30.

The T-junction IIbii with 20% bifurcation out of the branch pipe is shown in Fig.31 and with stream tracer in Fig.32. There is circulation in the branch pipe and a small vortex in the main pipe right after the bifurcation.

The T-junction IIc with equal split in the branch and main outlet is illustrated in Fig.34. From the stream tracer in Fig.35 it seems that the velocity up the main branch accelerates, and there is no visible flow in the main outlet.
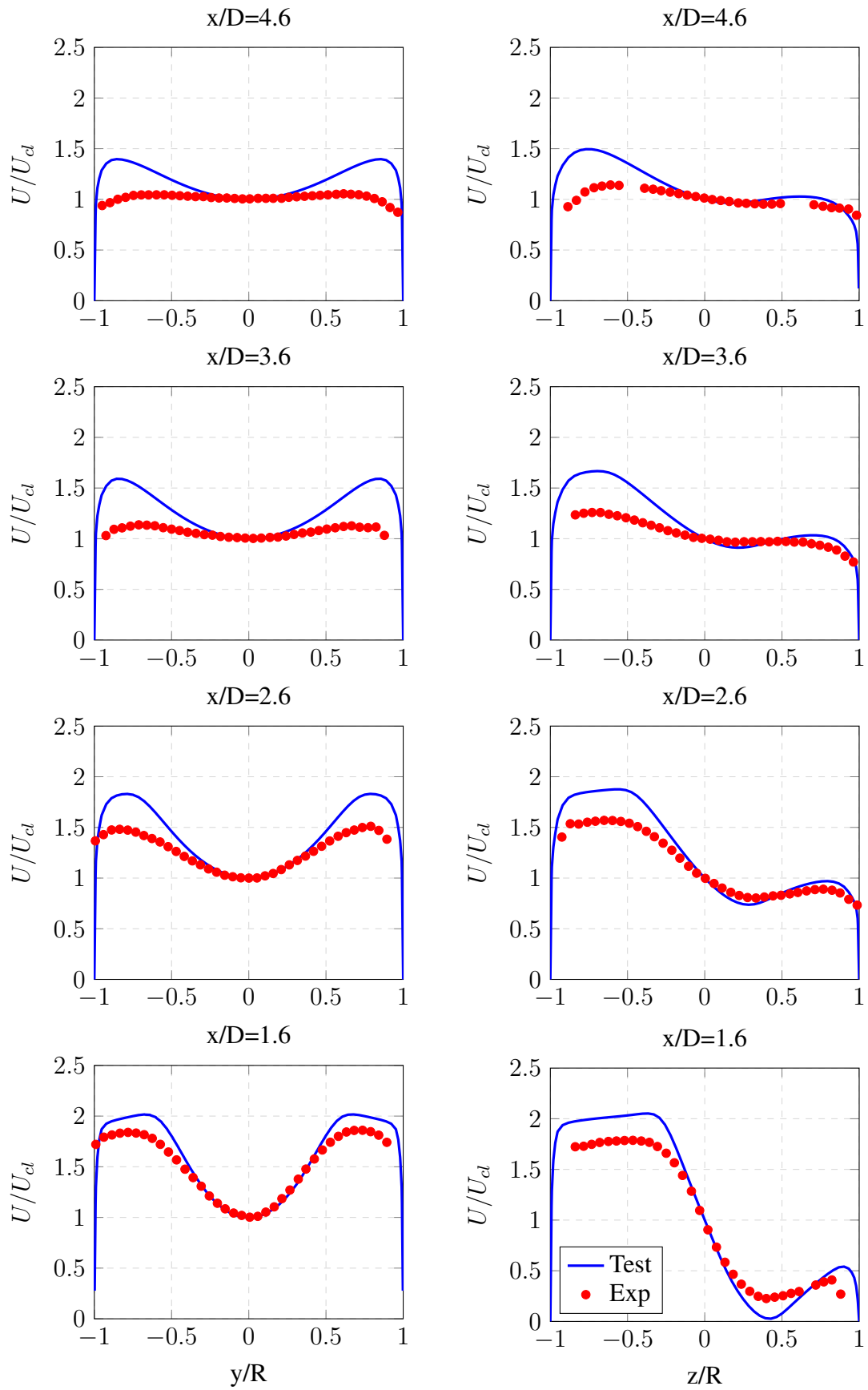
Figure 22: Mean axial velocity over the diameter, horizontal (left) and vertical (right
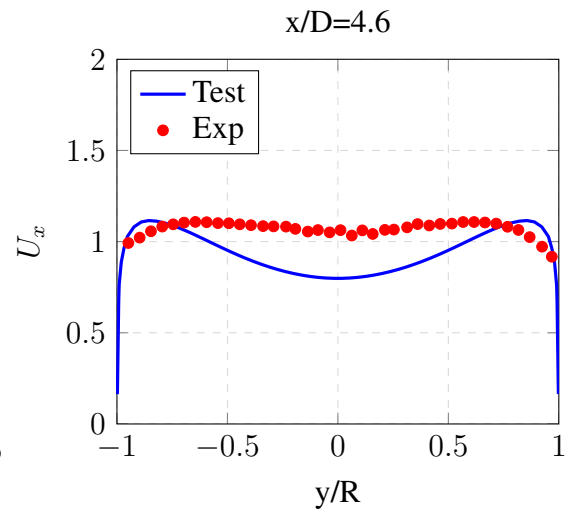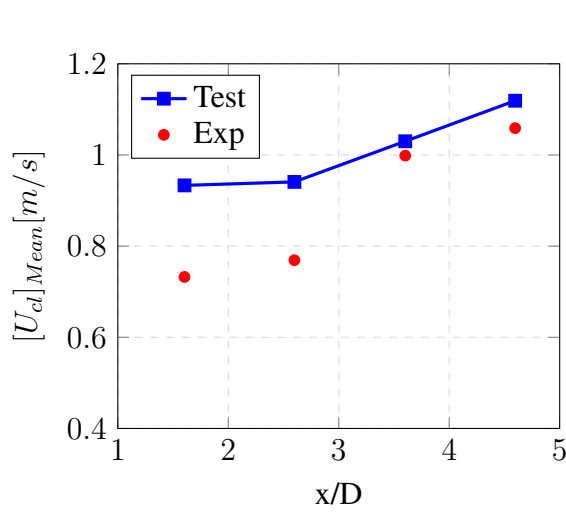
Figure 23: Mean of center line velocity

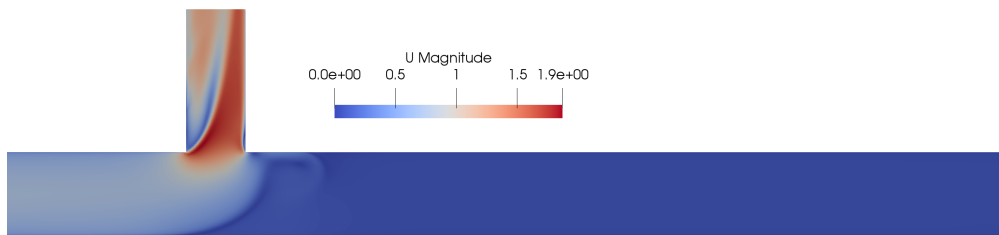Figure 24: Averaged streamwise velocity at 4.6 D

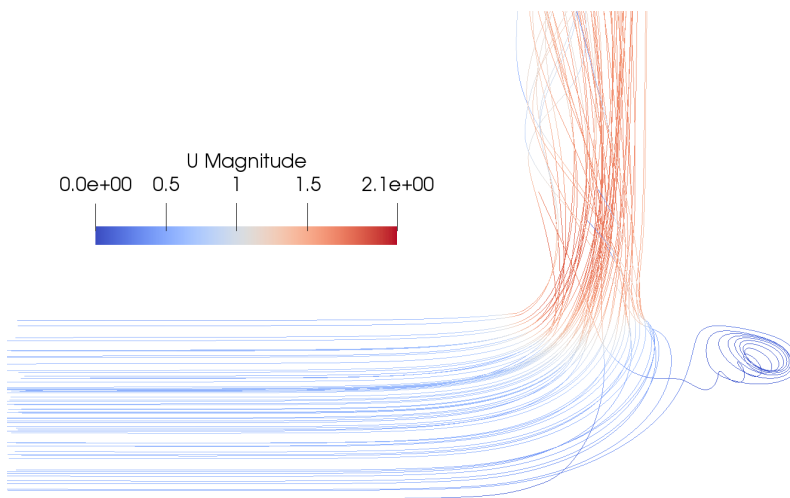Figure 25: Cross section velocity profile for T-Junction IIa

Figure 26: Stream trace for T-Junction IIa
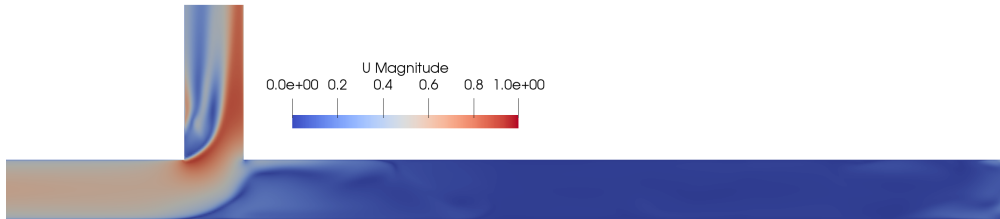
Figure 27: Surface lic for T-Junction IIa

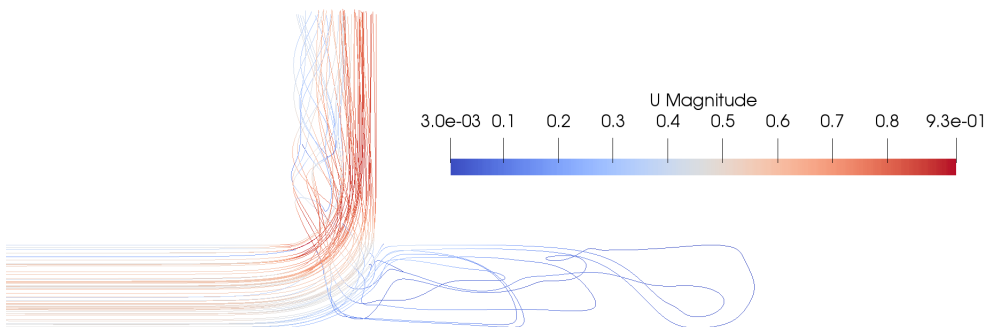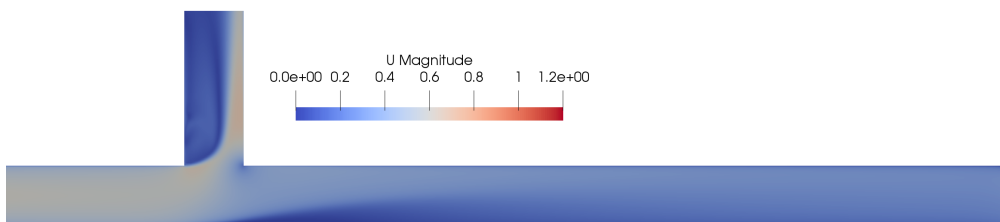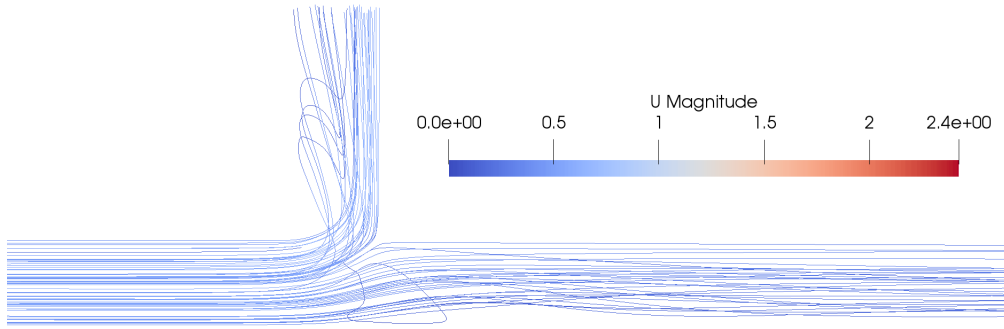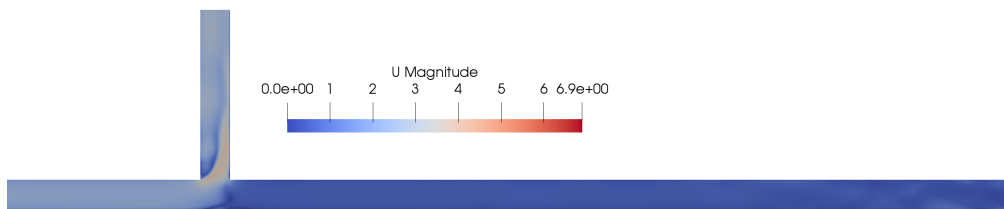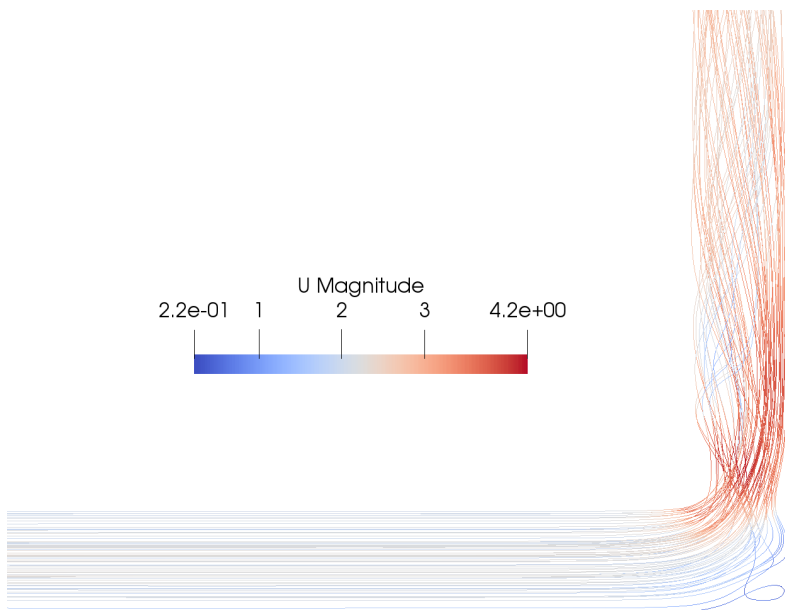Figure 28: Cross section velocity profile for T-Junction IIbi

Figure 29: Stream trace for T-Junction IIbi

Figure 30: Surface lic for T-Junction IIbi

Figure 31: Cross section velocity profile for T-Junction IIbii

Figure 32: Stream trace for T-Junction IIbii

Figure 33: Surface lic for T-Junction IIbii

Figure 34: Cross section velocity profile for T-Junction IIc

Figure 35: Stream trace for T-Junction IIc

Figure 36: Surface lic for T-Junction IIc

Beneš et al. [16] PIV measurements are illustrated in Fig.37 and in Fig.38 with numerical values from the simulation. The flow pattern for PIV in both cases is relatively close to the simulations. The flow streaming upwards is steeper in the beginning than for the experiment. The recirculation zone after the cross section is very prominent in the computation in Fig.37. There is also a more visible separation in the numerical cases, especially for the flow rate 0.6:0.4. Since there is only 20% flow in the branch pipe in Fig.38 the flow is obviously thinner and lays closer to the opposite wall. In Fig.38b the outward flow in the branch is much larger and gives an impression that the flow rate out of the branch is larger for the simulation than for the experiment.

For the case T-junction IIc, Sierra-Espinosa et al. [17], [18] investigated the turbulent flow with bifurcation in a 90^0 T-junction. The values from LDA are taken at the distances 1.1D and 1.04D in the branch pipe. The data are in Fig.39. Except for the rough estimation of the overall shape there are significant differences between the experiment and the simulation. At the distance 1.1D, the u_z velocity has a higher and wider peak, while the tail has an extra peak before the non-slip condition sets in. At the distance 1.04D the experimental data has a higher peak value, while the numerical values again give a wider peak. The tail seems to fit better at this distance compared to 1.1D. It is also worth mentioning that none of the numerical values from Sierra-Espinosa et al. seems to fit. The main peak on the left side was sharper and had a better fit, but the RANS SST $k - \omega$ model has a better fit at the tail at 1.04D than any of the other simulations in that case. It seems that this choice of model and solver does not give a good prediction of the velocity pattern in this particular case.
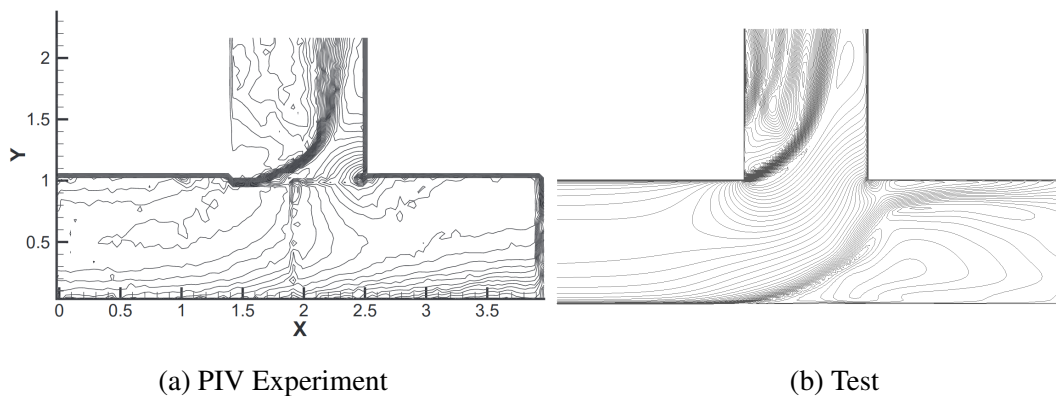

(a) PIV Experiment

(b) Test

Figure 37: Isolines from PIV experiment for T-junction IIbi. Flow rate 0.6:0.4
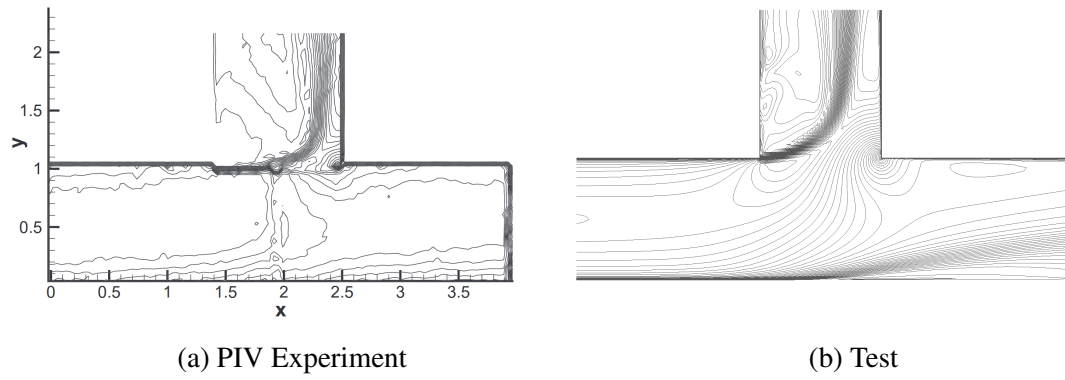
(a) PIV Experiment

(b) Test

Figure 38: Isolines from PIV experiment for T-junction IIbii. Flow rate 0.8:0.2
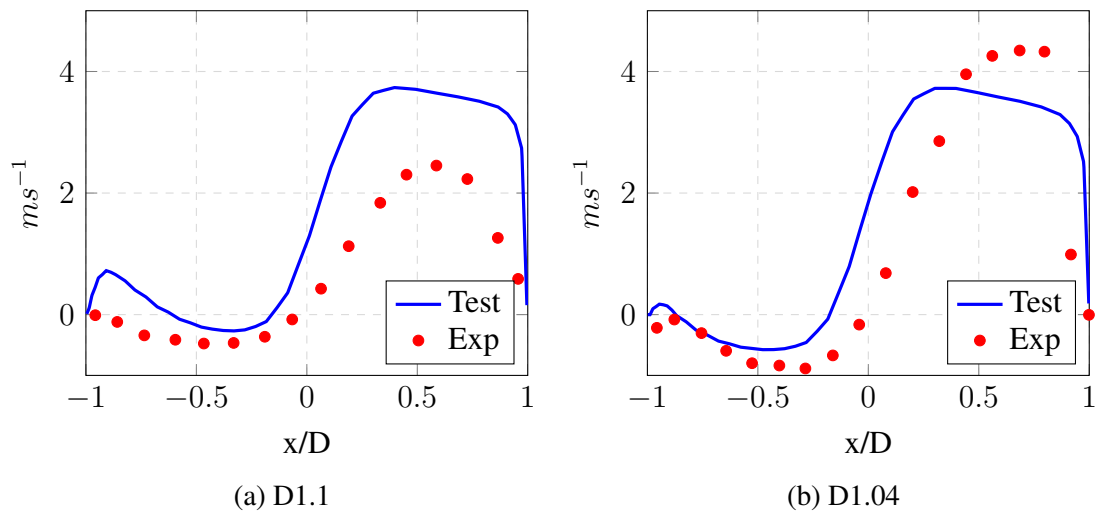

(a) D1.1

(b) D1.04

Figure 39: Velocity in the branch for T-junction IIc

8.4 T-junction III

For Fig.40, 41, 42a and 42b the T-junction IIIa case is visualised. The velocity at the inlet of the outlet branch shows the highest value in Fig.40, as expected due to the bending of the flow. The velocity in the main pipe between the branches is low, since the majority of the flow goes out of the branch before coming down the second branch, passing out in the main outlet. In Fig.41 the three recirculation zones, at the beginning of the outlet branch, between the two branches in the main pipe and after the inlet branch in the main pipe, are present as predicted. The recirculation zone after the branch inlet seems larger than for the T-junction I, so the mixing should be increased. The stream tracers in Fig.42a shows the flow leaking from the inlet over to the outlet of the main pipe. In Fig.42b the flow is represented with two different colours to better visualise the flow leaking over.

T-junction IIIb simulations of the flow are illustrated in Fig.44, 45 and 46. The recirculation zone shows a more defined vortex-shaped form between the branches and after the inlet branch in the main pipe, compared to T-junction IIIa.

In the surface lic of T-junction IIIc in Fig.49 the vortex in the middle of the branch is more compact than for the T-junction IIIb. The shape is more circular in IIIc. The flow pattern in the stream tracer is more disturbed in the IIIb case than for the IIIc. The circulation zone in the middle of the branch for case IIIc seems more defined than for the IIIb.

Since the distance between the branches in case IIId is also the shortest the circulation zone in Fig.52, 53 and 54 is understandably smaller, compared to the other cases. In Fig.55 the zones between the branches and right after the last branch seem more spread out and chaotic than in the other cases.

Table 24 shows the bulk velocity in the middle between the two branches of the main pipe. The value for the T-junction IIIa is the lowest, as expected due to the larger distance between the branches. As the distance between the branches gets shorter the value of the bulk velocity increases. When comparing the bulk velocity values between case IIIa, IIIb, IIIc and IIId it is seen that they are not equal. The smallest difference in value is between IIIb and IIIc. The distance
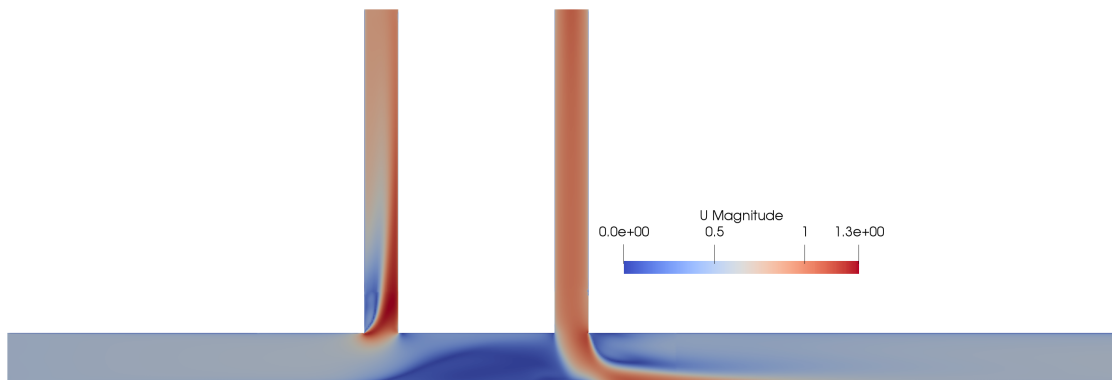

Figure 40: Velocity profile for TJIIIa

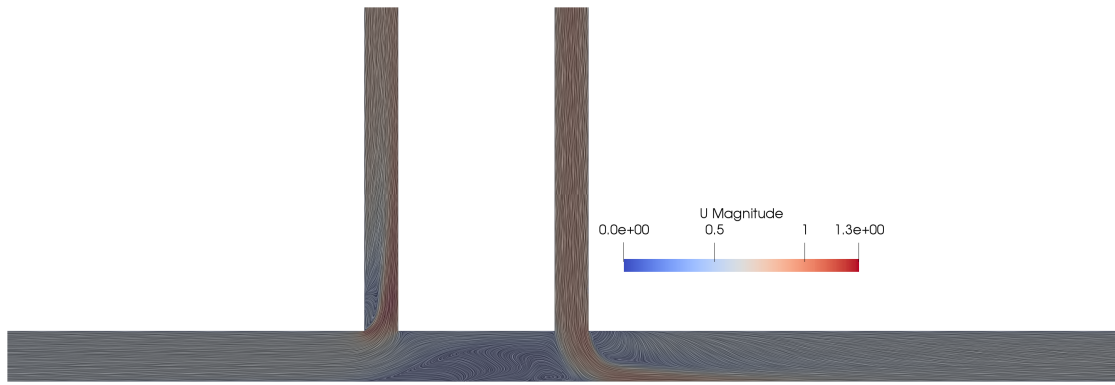Figure 41: Surface lic for T-Junction TJIIIa

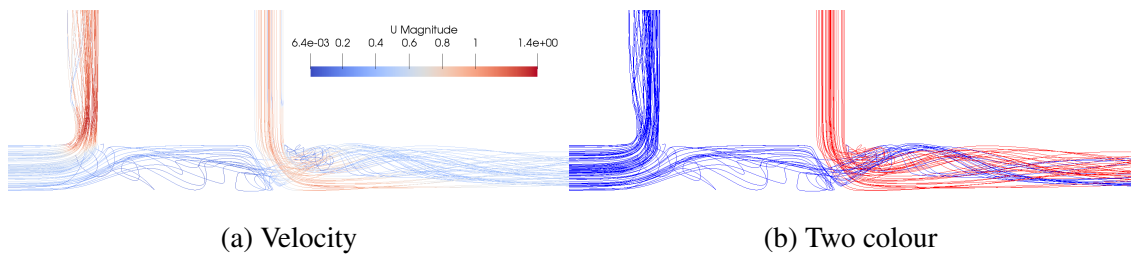(a) Velocity   (b) Two colour

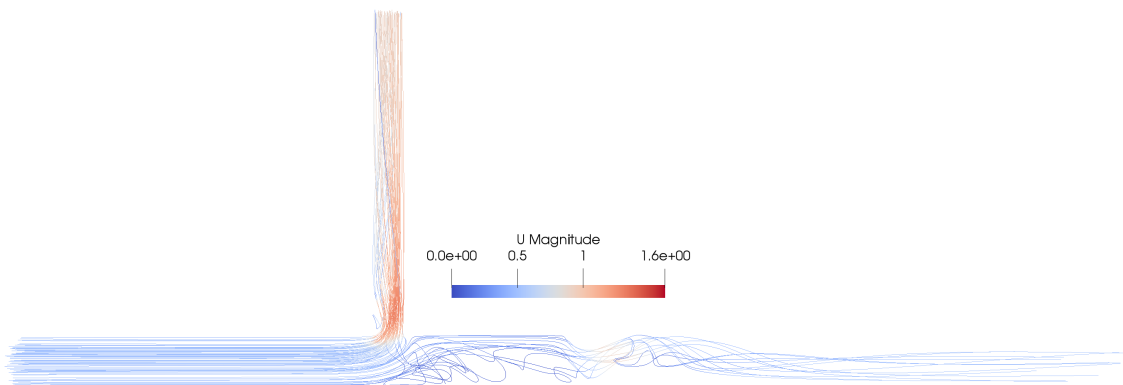Figure 42: Stream tracing for TJIIIa

Figure 43: Stream tracing for outlet1 only for TJIIIa

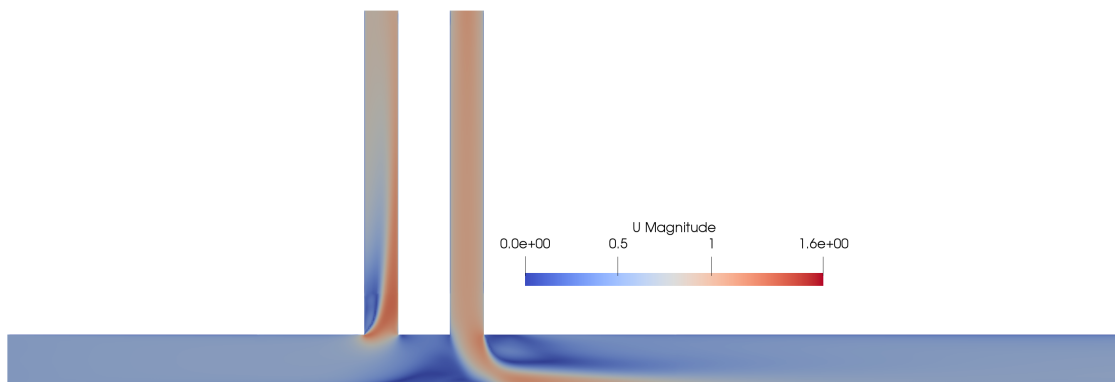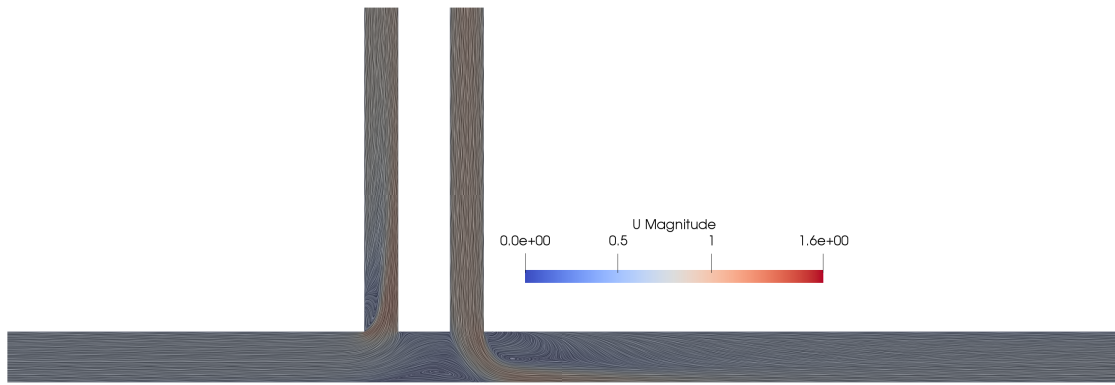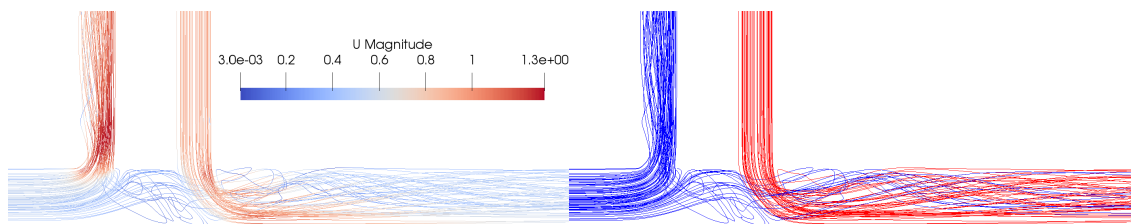

Figure 44: Velocity profile for TJIIIb

Figure 45: Surface lic for T-Junction TJIIIb

(a) Velocity   (b) Two colour

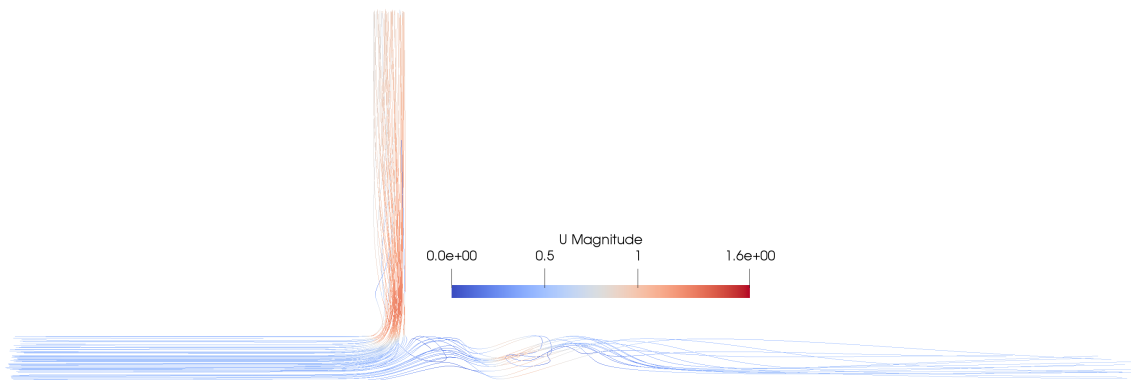Figure 46: Stream tracing for TJIIIb

Figure 47: Stream tracing for outlet1 only for TJIIIb
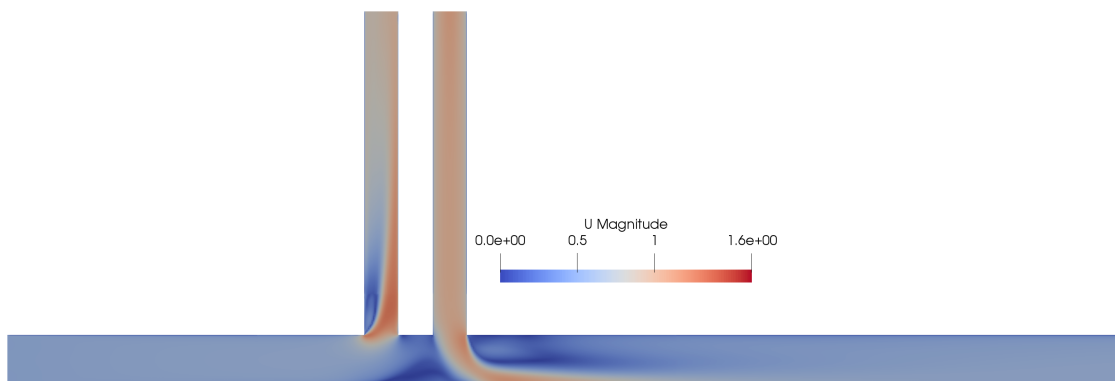

Figure 48: Velocity profile for TJIIIc

Figure 49: Surface lic for T-Junction TJIIIc

(a) Velocity   (b) Two colour

Figure 50: Stream tracing for TJIIIc

Figure 51: Stream tracing for outlet1 only for TJIIIc

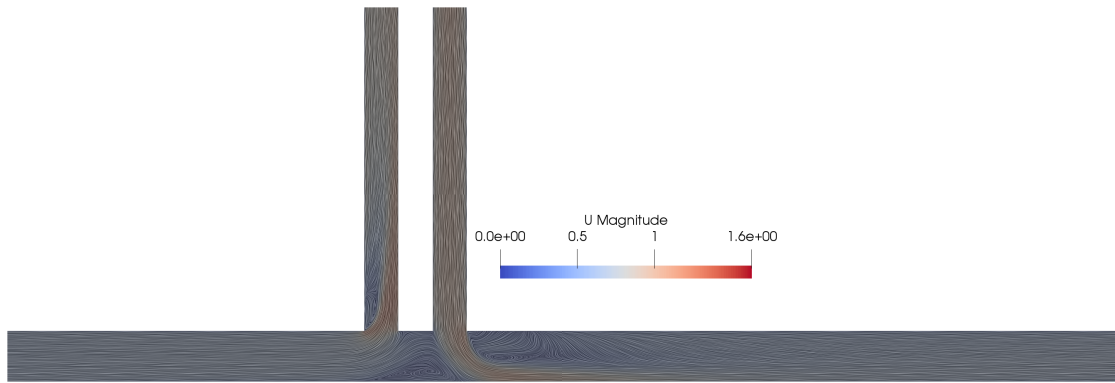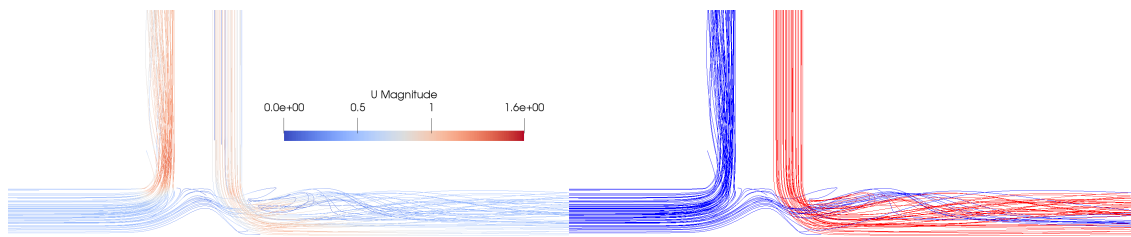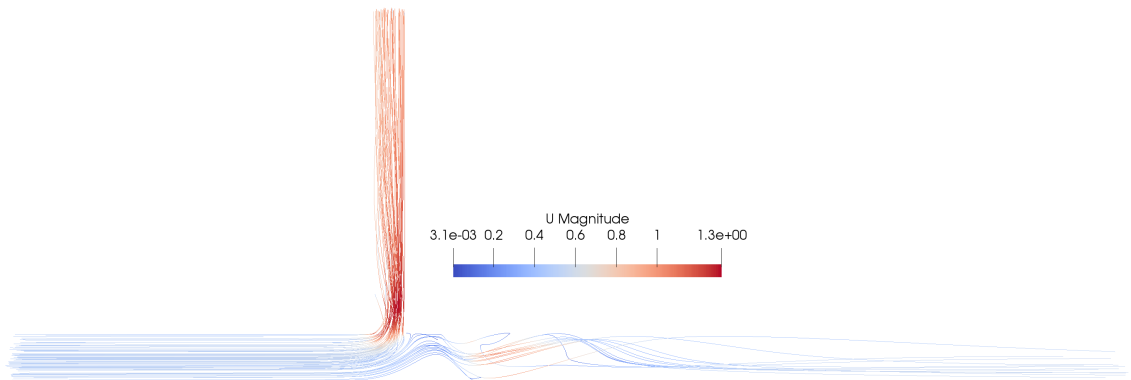Figure 52: Velocity profile for TJIIId

Figure 53: Surface lic for T-Junction TJIIId

(a) Velocity

(b) Two colour

Figure 54: Stream tracing for TJIIId

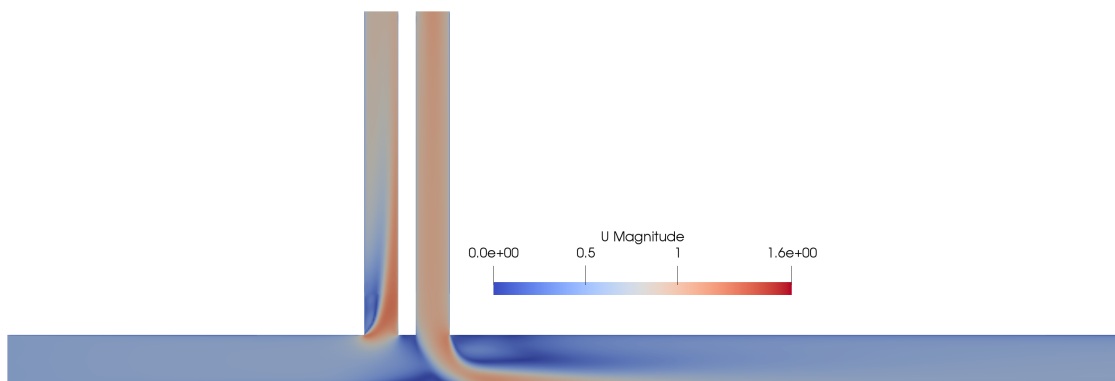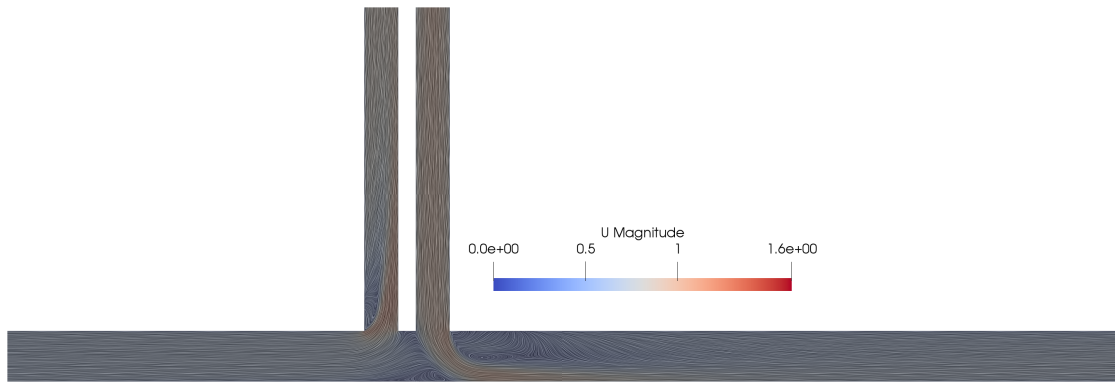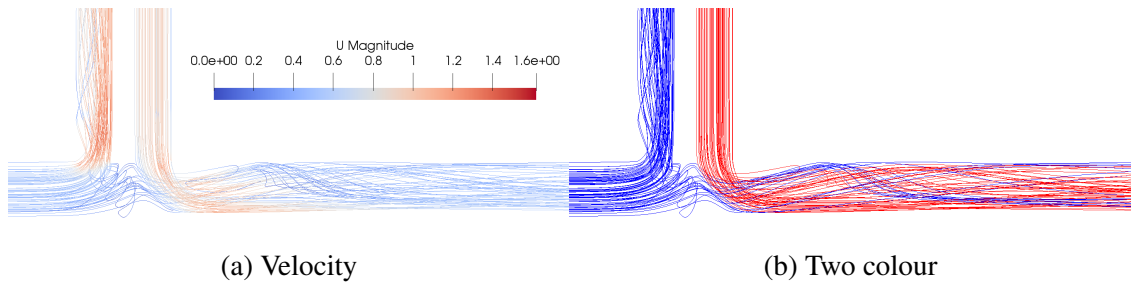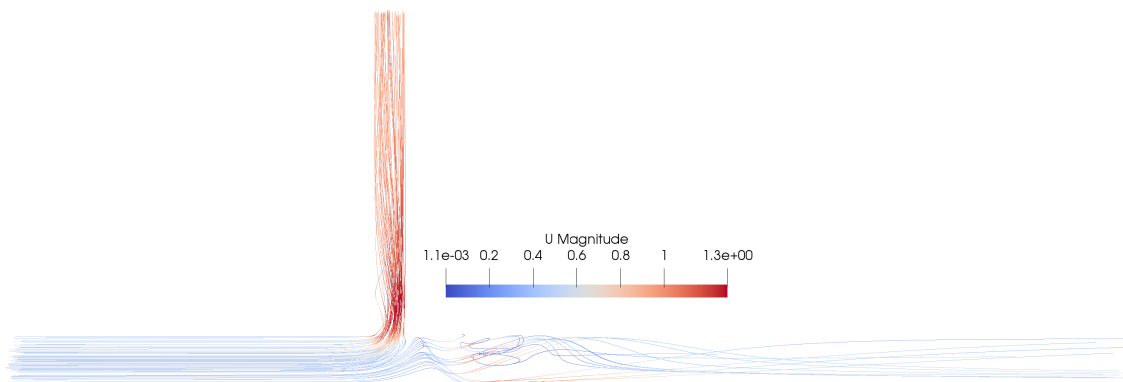Figure 55: Stream tracing for outlet1 only for TJIIId

between the branches in the cases IIIb, IIIc and IIId are the same, but the values of increased bulk velocities are not the same. That would indicate that the distance between the branches in case IIId is too short, something that would lead to a too high interference with the recirculation zone. When the second branch comes too close to the recirculation zone after the outlet branch it interferes with the vortex and will extract a larger amount of flow directly over the middle part of the main pipe.

The negative values of u_x velocity will give an indication on the recirculation zone. The lower the value the less recirculation.

Table 25 list the summation of the negative u_x values right before the second branch. Between the case TJIIIb and TJIIIc has the smallest difference in the negative u_x value, which could be interpreted as the recirculation between the branches are within that given distance.

To get at better estimation and understanding of the flow between the branches it would be preferable to have more data/cases to compare with.

Extracted from this, it seems that a distance of 2-2.5D between the branches gives the best result, with less interference between the branches, when comparing to case IIIb, IIIc and IIId.

Another parameter that would have a significant impact on the flow is rounding of the branch edges.

Both Costa et al.[19] and Sierra-Espinosa et al. [17], [18] investigated the effect of a 90^0 T-junction with edge rounding to the branch pipe. Sierra-Espinosa et al. focused on the the difference between experimental values with different models and solvers. Costa et al. were more focused on the effect of the rounding of the edge to the branch pipe.

Table 24: Bulk velocities between the branches for T-junction III

IIIa	IIIb	IIIc	IIId
5.16631	5.37204	5.51107	6.32742

Table 25: Sum of negative u_x values for T-junction III

IIIa	IIIb	IIIc	IIId
-28.74	-62.55	-70.51	-83.13

9   Conclusion

This Master thesis investigates the applicability of RANS SST $k - \omega$ model on different sets of T-junctions and the effect the distance between two branches in the T-junction will have on each other. Gether AS, as many other business, uses different configurations of T-junctions in their products. It is therefore important to get a better understanding of the fluid behaviour in the T-junctions and ways to simulate these in a cost-efficient way.

The RANS model requires much less computational cost than LES and DNS, but it is usually less accurate. The SST $k - \omega$ model, due to its hybrid between $k - \epsilon$ behaviour in the free stream and $k - \omega$ behaviour in the near wall region, makes it a suitable match for these simulations, and it performs well in separate flow.

It is concluded that the RANS SST $k - \omega$ model gives results that are satisfactory for this case.

This paper has investigated the importance of making and applying a grid in order to approach an optimal resolution of cells and layers to obtaining the final solution. It is important to balance the computational cost with the accuracy, even for simple geometry as a T-junction.

The investigations of the double T-junction look into the effect of the distance between the branches and conclude that a distance of 2-2.5D between the branches gives the best results in case IIIb, IIIc and IIId, with less interference between the branches.

References

[1] G. AS. (). Gether as, [Online]. Available: http://www.gether.no/. (accessed: 08.04.2019).

[2] H. K. Versteeg and W. Malalasekera, *An Introduction to Computational Fluid Dynamics The Finite Volume Method, second edition*. Pearson Education Limited, 2007, ISBN: 978-0-13-127498-3.

[3] B. Smith, J. Mahaffy, and K. Angele, "A cfd benchmarking exercise based on flow mixing in a t-junction," *Nuclear Engineering and Design*, vol. 264, pp. 80–88, 2013, SI:NURETH-14, ISSN: 0029-5493. DOI: https://doi.org/10.1016/j.nucengdes.2013.02.030. [Online]. Available: http://www.sciencedirect.com/science/article/pii/S0029549313000897.

[4] C. Online. (). Linear eddy viscosity models, [Online]. Available: https://www.cfd-online.com/Wiki/Linear_eddy_viscosity_models. (accessed: 29.05.2019).

[5] B. Launder and D. Spalding, "The numerical computation of turbulent flows," *Computer Methods in Applied Mechanics and Engineering*, vol. 3, no. 2, pp. 269–289, 1974, ISSN: 0045-7825. DOI: https://doi.org/10.1016/0045-7825(74)90029-2. [Online]. Available: http://www.sciencedirect.com/science/article/pii/0045782574900292.

[6] D. C. WILCOX, "Reassessment of the scale-determining equation for advanced turbulence models," *AIAA Journal*, vol. 26, pp. 1299–1310, Nov. 1988. DOI: 10.2514/3.10041.

[7] D. Wilcox, "Comparison of two-equation turbulence models for boundary layers with pressure gradient," *AIAA Journal*, vol. 31, Aug. 1993. DOI: 10.2514/3.11790.

[8] D. C. Wilcox, *Turbulence modelling for CFD*. DCW Industries, La Cañada, 1993.

[9] D. Wilcox, "Simulation of transition with a two-equation turbulence model," *Aiaa Journal - AIAA J*, vol. 32, pp. 247–255, Feb. 1994. DOI: 10.2514/3.59994.

[10] F. Menter, "Performance of popular turbulence model for attached and separated adverse pressure gradient flows," *AIAA Journal*, vol. 30, Sep. 1992. DOI: 10.2514/3.11180.

[11] ——, "Improved two-equation k-omega turbulence models for aerodynamic flows," *NASA STI/Recon Technical Report N*, vol. 93, Nov. 1992.

[12] ——, "Two-equation eddy-viscosity transport turbulence model for engineering applications. aiaa journal 32(8), 1598-1605," *AIAA Journal*, vol. 32, Sep. 1994. DOI: 10.2514/3.12149.

[13] F. R. Menter, "Eddy viscosity transport equations and their relation to the k-e model," *Journal of Fluids Engineering*, vol. 119, no. 4, pp. 876–884, Dec. 1997, ISSN: 0098-2202. DOI: 10.1115/1.2819511. [Online]. Available: http://dx.doi.org/10.1115/1.2819511.

[14] F. Menter, M. Kuntz, and R. Langtry, "Ten years of industrial experience with the sst turbulence model," *Heat and Mass Transfer*, vol. 4, Jan. 2003.

[15] C. Direct. (). Openfoam v6 user guide: 4.5 solution and algorithm control, [Online]. Available: https://cfd.direct/openfoam/user-guide/v6-fvsolution/. (accessed: 23.05.2019).

[16] L. Beneš, P. Louda, K. Kozel, R. Keslerová, and J. Štigler, "Numerical simulations of flow through channels with t-junction," *Applied Mathematics and Computation*, vol. 219, no. 13, pp. 7225–7235, 2013, ESCO 2010 Conference in Pilsen, June 21- 25, 2010, ISSN: 0096-

3003. DOI: https://doi.org/10.1016/j.amc.2011.04.074. [Online]. Available: http://www.sciencedirect.com/science/article/pii/S0096300311006448.

[17] F. Sierra-Espinosa, C. Bates, and T. O'Doherty, "Turbulent flow in a 90 pipe junction: Part 1: Decay of fluctuations upstream the flow bifurcation," *Computers Fluids*, vol. 29, no. 2, pp. 197–213, 2000, ISSN: 0045-7930. DOI: https://doi.org/10.1016/S0045-7930(99)00004-3. [Online]. Available: http://www.sciencedirect.com/science/article/pii/S0045793099000043.

[18] F. Sierra-Espinosa, C. Bates, and T. O'Doherty, "Turbulent flow in a 90 pipe junction: Part 2: Reverse flow at the branch exit," *Computers Fluids*, vol. 29, no. 2, pp. 215–233, 2000, ISSN: 0045-7930. DOI: https://doi.org/10.1016/S0045-7930(99)00005-5. [Online]. Available: http://www.sciencedirect.com/science/article/pii/S0045793099000055.

[19] N. P. Costa, R. Maia, F. Pinho, and M. Proença, "Edge effects on the flow characteristics in a 90 deg tee junction," *Journal of Fluids Engineering-transactions of The Asme - J FLUID ENG*, vol. 128, Apr. 2006. DOI: 10.1115/1.2354524.

[20] T. Höhne, "Scale resolved simulations of the oecd/nea–vattenfall t-junction benchmark," *Nuclear Engineering and Design*, vol. 269, pp. 149–154, Apr. 2014. DOI: 10.1016/j.nucengdes.2013.08.021.

[21] H. Ayhan and C. N. Sökmen, "Cfd modeling of thermal mixing in a t-junction geometry using les model," *Nuclear Engineering and Design*, vol. 253, pp. 183–191, 2012. DOI: 10.1016/j.nucengdes.2012.08.010. [Online]. Available: https://app.dimensions.ai/details/publication/pub.1036601668.